Title: Retinal image assessment using bi-level adaptive morphological component analysis

Authors: Malihe Javidi, Ahad Harati, HamidReza Pourreza

PII: S0933-3657(18)30337-3
DOI: https://doi.org/10.1016/j.artmed.2019.07.010
Reference: ARTMED 1702

To appear in: *ARTMED*

Received date: 25 July 2018
Revised date: 25 July 2019
Accepted date: 26 July 2019

Please cite this article as: Javidi M, Harati A, Pourreza H, Retinal image assessment using bi-level adaptive morphological component analysis, *Artificial Intelligence In Medicine* (2019), https://doi.org/10.1016/j.artmed.2019.07.010

Retinal image assessment using bi-level adaptive morphological component analysis

Malihe Javidi† m.javidi@qiet.ac.ir Ahad Harati†† a.harati@um.ac.ir HamidRezaPourreza††hpourreza@um.ac.ir

†Computer Engineering Department, Quchan University of Advanced Technology, Quchan, Iran

†† Department of Computer Engineering, Ferdowsi University of Mashhad, Mashhad, Iran

Highlights

- Our method analyzes retinal image to extract diagnostically helpful components of the retinal image.
- These components are considered very important in clinical decision making such as checking patient status, type and duration of treatment.
- This method is based on extension of MCA algorithm which benefits from the adaptive representation obtained via dictionary learning.
- Reported results confirmed the effectiveness of the proposed method in the separation of vessel and exudate components especially in retinal images with proliferating DR.

Abstract

The automated analysis of retinal images is a widely researched area which can help to diagnose several diseases like diabetic retinopathy in early stages of the disease. More specifically, separation of vessels and lesions is very critical as features of these structures are directly related to the diagnosis and treatment process of diabetic retinopathy. The complexity of the retinal image contents especially in images with severe diabetic retinopathy makes detection of vascular structure and lesions difficult. In this paper, a novel framework based on morphological component analysis (MCA) is presented which benefits from the adaptive representations obtained via dictionary learning. In the proposed Bi-level Adaptive MCA (BAMCA), MCA is extended to locally deal with sparse representation of the retinal images at patch level whereas the decomposition process occurs globally at the image level. BAMCA method with appropriately offline learnt dictionaries is adopted to work on retinal images with severe diabetic retinopathy in order to simultaneously separate vessels and exudate lesions as diagnostically useful morphological components. To obtain the appropriate dictionaries, K-SVD dictionary learning algorithm is modified to use a gated error which guides the process toward learning the main structures of the retinal images using vessel or lesion maps. Computational efficiency of the proposed framework is also increased significantly through some improvement leading to noticeable reduction in run time.

We experimentally show how effective dictionaries can be learnt which help BAMCA to successfully separate exudate and vessel components from retinal images even in severe cases of diabetic retinopathy. In this paper, in addition to visual qualitative assessment, the performance of the proposed method is quantitatively measured in the framework of vessel and exudate segmentation. The reported experimental results on public datasets demonstrate that the obtained components can be used to achieve competitive results with regard to the state-of-the-art vessel and exudate segmentation methods.

Keywords – Bi-level adaptive morphological component analysis, Dictionary learning, Diabetic retinopathy image assessment.

1 Introduction

Diabetic retinopathy (DR) is a diabetic complication which can lead to the visual impairment or even blindness if not treated in a timely manner. DR is a salient and progressive disease so early diagnosis and treatment is of crucial importance for effective cure. The ophthalmologists grade DR and determine the special treatment based on the type and location of the vessel and lesions. Recently, deep learning has been introduced as a powerful tool for automatic DR grading. Deep networks, trained on large enough datasets, are able to directly grade DR stages, but they do not provide any human usable clue why an image is graded to the selected class, and also do not output type and position of the present lesions.

In clinical research, blood vessel segmentation is considered as a prerequisite step for the analysis of vessel parameters such as length, width and tortuosity. On the other hand, the main problem of traditional vessel segmentation algorithms is producing false positive vessels in the images with lesions. Therefore, automatic segmentation of vessels and lesions is very critical in DR diagnosis. As an example, detection of lesions such as exudates and their relation to the fovea is an important factor in determining the need for either systemic or ocular treatments [1], [2].

Therefore, in this paper, we consider problem of separating diagnostically important components of the retinal images which can be very useful in different medical aspects such as diagnosis, treatment process and even educating resident ophthalmologists. Such components can be used in more specific DR treatments such as detection of pigmentary retinopathy and determination its progression status [3] or simply as preprocessing step toward vessel/lesion segmentation.

Recently sparse representation has produced promising outcomes in vessel and exudate segmentation algorithms [4]–[7]. Sparse representation classifier along with pre-determined dictionaries is utilized by Zhang et al. [4] to classify vessel and non-vessel image patches. In our previous work [5], we extended this approach using discriminative dictionary learning (DDL) within a sparse representation framework. Despite the success of this approach, mainly resulted from the flexibility of the learned dictionaries, DDL methods do not have the capability to create generative models in order to obtain components of the input signals. In fact, the representation obtained by DDL can be used in tasks such as classification but cannot be used to generate output images for further analysis by ophthalmologist experts or automatic screening systems. To obtain generative models useful for such purposes, we propose a framework based on morphological component analysis (MCA) algorithm and sparse representation.

MCA is an iterative thresholding procedure which decomposes the input image into its morphological components but traditionally is used along with transform representations such as DCT (discrete cosine transform) or wavelet transform. Previously, we adopted MCA using shearlet and contourlet transforms which can cope well with representing vessel and lesion contents of the retinal images [6], [7]. MCA may effectively decompose normal and healthy retinal images when used with pre-determined dictionaries. However, as DR affects the retina more and more, the performance of this method degrades. In fact, the fixed dictionaries no longer can represent signal components well enough for separation. Therefore, component separation in retinal images with severe DR needs more efforts.

This motivates us to use generative modeling of MCA alongside the adaptive representation obtained via dictionary learning. Peyre et al. [8] also proposed adaptive MCA using predetermined global dictionaries alongside local learnt dictionaries. They combine the process of image decomposition and dictionary learning in a single global optimization problem. However, using limited number of training samples and facing large number of unknown parameters in multiple dictionaries may lead to suboptimal

solution or even cause divergence. In this paper, we propose a novel framework, called Bi-level Adaptive MCA (BAMCA), to work on retinal image patches with severe DR in order to extract vessels and exudate lesions as diagnostically helpful components of the input image.

Recently, utilizing dictionary learning within MCA has yielded promising results in variety of applications including clutter reduction [9], [10], noise suppression in low dose computed tomography (LDCT) images [11], text detection [12], separation of interference stripes in hyperspectral images [13] or analysis of painting X-ray images [14]. In all these applications, it was possible to learn a separate dictionary for each source component using a sequence of images that only contains corresponding component. However, in our case where training samples of each component are not available separately, using this method is impossible. Therefore, we adapt the dictionary learning process to use binary maps of lesion and vessels alongside the original retinal images in order to obtain the dictionaries offline. In fact, for learning the vessel and exudate dictionaries in the proposed BAMCA framework, K-SVD (K-singular value decomposition) algorithm [15] is modified to use a gated error which considers the foreground containing main structures (vessel or exudate) of the retinal image and discards the noisy background.

In the proposed framework, the sparse representation of input image is obtained locally at patch level whereas the decomposition process occurs globally at the image level. In fact, BAMCA iteratively cycles between local competitions among atoms from different dictionaries within each patch, and a global competition among the coefficients at image level to determine their contributions for each component. For this purpose, the coefficients of all patches over both dictionaries are computed (local phase), the appropriate value for the MCA threshold is determined based on an image level competition which combines the collective effects of local patch representations within the overlapping regions (global phase).

The rest of the paper is organized as follows. Section II, gives a literature review of the vessel and exudate detection in retinal image. In Section III, the concept of MCA is briefly reviewed. A description of the proposed BAMCA method, the way that MCA and dictionary learning is applied to separate vessels from exudate lesions, is provided in Section IV. Experimental results are presented in Section V and discussed in Section VI. Finally Section VII draws conclusion and future work.

2 Literature review of vessel and exudate segmentation

A review of existing methods for blood vessel and exudate detection is presented in the literature [16], [17]. Some of these methods will be briefly summarized in this section.

Tracking based methods are the first methods for vessel segmentation. In these methods, the vessel map segmented by tracing vessels from some seed points and following them using local information [18], [19]. In the match filter methods, a series of different Gaussian shape filters are employed to detect blood vessels [20]–[23]. Wavelet and Gabor transforms [24]–[26] are other methods used to enhance blood vessel detection with different thicknesses and orientations. Azzopardi et al. [27] also applied a combination of shifted filter responses (COSFIRE) for vessel segmentation. Multiscale approaches are aimed at producing vessel with varying widths [28]. Vlachos and Dermatas [29] combined the multiscale line tracking results and quantized them to achieve the final vessel map. Vessel detection method based on complex continuous wavelet transform [30] was proposed to represent vessel structure in different scales and directions. Nguyen et al. [31] proposed vessel detection method based on line detection. In [32] vesselness and Hessian multiscale enhancement filters were applied for automatic detection of vessels.

Recently, unsupervised and supervised methods for vessel segmentation have attracted considerable attention. The approaches based on unsupervised methods attempt to achieve the inherent features of blood vessels without contribute directly the ground truths [33], [34]. In supervised methods, each image pixel is represented by a feature vector then a supervised classifier is trained to determine that a pixel belongs to vessel or not [35]–[38]. Sparse representation-based classifier has been successfully applied to vessel segmentation by Zhang et al. [4]. They proposed a vessel segmentation method based on multiscale production of matched filters and sparse representation-based classifier. In contrast to this approach which depends on fixed dictionaries, the vessel segmentation algorithm based on discriminative dictionary learning and sparse representation was proposed in [5]. In this method, two discriminative dictionaries for vessel and non-vessel image patches were learned, and then a voting scheme was utilized to generate the binary vessel map. A novel framework based on MCA algorithm using fix dictionaries was presented in [6], [7]. In this method, MCA algorithm with non-subsampled shearlet transform and non-subsampled contourlet transform was adopted to separate vessels and lesions from each other.

Besides these approaches, vessel segmentation methods were proposed based on applying morphological operations [39], [40] and explicit vessel models [41], [42]. Siva and Vasuki [43] proposed vessel segmentation method using binary morphological operations and templates illustrated by Soares [38]. The overall accuracy of their method was increased with the removal of the optic disc region using anisotropic diffusion filter.

Main exudate detection algorithms can be classified into four categories: (1) Pattern recognition, (2) mathematical morphology, (3) region growing and (4) thresholding-based approaches.

Sopharak et al. [44] proposed a method for exudate detection using fuzzy C-means clustering algorithm. A combination of fuzzy C-means algorithm, genetic algorithm and neural network has been applied to segment exudate by Osareh et al. [45]. Figueiredo et al. [46] extracted the multiscale features based on wavelet and Hessian multiscale analysis then detected several lesions from retinal images with appropriate binary classifiers. A visual words dictionary representing points of interest within the fundus image was constructed by speeded up robust features and k-means clustering [47]. Using this dictionary and a quantization process, each image was represented by a signature of the visual words it contains, and then classified as a normal or abnormal image by SVM (support vector machine). Other related approaches used Bayesian classifier [48] and Gaussian mixture model [49] to improve the exudate detection algorithm. Liu et al. [50] described the structure of the exudates using the histogram of completed local binary patterns and then classified them with a random forest classifier.

Some approaches used morphological operators to obtain the exudate map. Walter et al. [51] used the grey level image variation to find exudate lesions and then determined their contours by means of morphological reconstruction technique. Welfer et al. [52] proposed a coarse-to-fine strategy based on morphological reconstruction, regional minima detection and H-maxima transformation for exudate segmentation. Harangi and Hajdu [53] introduced a method based on mathematical morphology and active contours to detect precise exudates. In Zhang et al. [54] method, all exudate candidates were detected using morphological operators then each lesion was classified based on classical and contextual features.

Region growing methods segment the image based on homogeneity features. To detect exudates, Sinthanayothin et al. [55] introduced a method which was a combination of the recursive region growing

algorithm and a new technique, termed a Moat operator. Li and Chutatape [56] combined region growing algorithm and canny edge detector for exudate detection.

Local or global gray level analysis was used for exudate detection in thresholding based approaches. Sánchez et al. [57] presented a thresholding algorithm based on statistical mixture models. Then a post-processing method based on edge detection was applied to distinguish exudates from other bright lesions. A method based on applying a threshold on distance map belonged to an atlas image was developed by Ali et al. [58]. A thresholding method and ant colony optimization were combined to segment exudate regions by Pereira et al. [59]. García et al. [60] applied a method based on global and adaptive thresholding algorithms to obtain the lesion candidates. They extracted a group of features from candidates then employed radial basis function classifier to determine the true positive regions.

Recently, deep learning has been introduced as a powerful tool for many image related problems including DR screening [61]–[65]. In 2015, the California healthcare foundation put Kaggle competition with the goal to design an automated system for DR grading. All of the top teams in the challenge trained Convolutional Neural Networks (CNNs) to grade the severity of DR in 5 levels [66]. Ranking in the Kaggle competition was based on quadratic weighted Kappa score [67]. The winning teams in this challenge achieve high Kappa scores and their performance was comparable with an ophthalmologist grading. Nevertheless, there are some limitations which arise from the nature of deep networks. Training very large networks with many parameters requires great learning costs in terms of preparing numerous training samples and computation time [64], [68].

Furthermore, such networks are usually just provided with the image and the associated grade in the training phase and hence, their output does not contain any explicit detection and recognition of diagnostically helpful components such as microaneurysm, exudate or vessel features. These components are considered very important in clinical decision making such as checking patient status, type and duration of treatment. However, quite recently few researchers try to obtain segmentation maps for vessels [69]–[71] or lesions [62], [72]. Melinscak et al. [69] applied deep max-pooling convolutional neural networks (MPCNN) proposed by [73] to segment blood vessels, while Maji et al. [70] used an ensemble of CNNs for this purpose. Finally, Li et al. [71] remodels the segmentation algorithm as a problem of cross-modality data transformation from retinal images to vessel maps using deep networks. All these vessel segmentation methods process the input image patch by patch, using deep networks. This strategy shrinks the network size and makes training possible using tens of thousands training patches which can be extracted from the available datasets that only contain few tens images accompanied with the ground truth vessel maps. In the case of lesion detection, Yang et al. [74] uses a similar patch based strategy to detect different lesion types while Quellec et al. [62] and Gondal et al. [75] applies a Kaggle winner architecture [76] to obtain segmentation maps for different lesion types. In the following, we will compare our method against these state-of-the-art deep learning based approaches.

3 Image decomposition using MCA

The task of decomposing signals into their building components has attracted a growing attention to signal and image processing. A novel decomposition method called MCA that is based on sparse representation and different morphological diversity of signals has been presented by Starck et al. [77]–[79]. MCA assumed that each signal is a linear mixture of different components which are morphologically distinct.

Assumed that the signal $\mathbf{s} \in R^M$ is the linear mixture of K morphological components $\mathbf{y}_k$and it can possibly contain noise ε with standard deviation σ_ϵ:

$$\mathbf{s} = \sum_{k=1}^{K} \mathbf{y}_k + \varepsilon \qquad \sigma_\varepsilon^2 = var[\varepsilon] < +\infty \tag{1}$$

The aim of MCA framework is recovering all components $\{\mathbf{y}_k\}_{k=1}^K$ from their observed linear mixture which is an ill-posed inverse problem. Each component $\mathbf{y}_k$ can be sparsely represented in an associated sub-dictionary $\mathbf{\Phi}_k$ as:

$$\mathbf{y}_k = \mathbf{\Phi}_k \mathbf{x}_k \qquad k = 1. \ldots . K \tag{2}$$

where $\mathbf{x}_k$ is a sparse coefficient vector that only a few coefficients are large. A concatenated dictionary $[\mathbf{\Phi}_1. \ldots . \mathbf{\Phi}_k]$ can be developed in a way that the sub-dictionary $\mathbf{\Phi}_k$ can be sparsely represented the component $\mathbf{y}_k$ while inefficient (not as sparse) in representing the other components $\mathbf{y}_l$ for $l \neq k$. In the traditional MCA, the analytical transforms such as wavelet, curvelet, contourlet, sheerlet transforms are used as dictionaries to sparsely represent the source components. To characterize the complex components of the signal, another possible approach is using dictionary learning framework. The dictionaries generated by this approach are generally more fitted to the data.

In [77], [78], a method for estimating the components $\{\mathbf{y}_k\}_{k=1}^K$ has been proposed which is based on solving the following optimization problem:

$$\min_{\mathbf{x}_1 \ldots . \mathbf{x}_k} \sum_{k=1}^{K} \|\mathbf{x}_k\|_p^p \qquad s.t. \left\| \mathbf{s} - \sum_{k=1}^{K} \mathbf{\Phi}_k \mathbf{x}_k \right\|_2^2 \leq \sigma^2 \tag{3}$$

where $\|\mathbf{x}\|_p^p$ is the sparsity term and σ is typically chosen as $\tau\sigma_\epsilon$, where σ_ϵ is the noise standard deviation and τ is a constant. The constraint is related to the presence of noise. A similar objective could alternatively be written as:

$$\min_{\mathbf{x}_1 \ldots . \mathbf{x}_k} \frac{1}{2} \left\| \mathbf{s} - \sum_{k=1}^{K} \mathbf{\Phi}_k \mathbf{x}_k \right\|_2^2 + \lambda \sum_{k=1}^{K} \|\mathbf{x}_k\|_p^p \tag{4}$$

where λ is a regularization parameter. Generally, finding a solution to problem (4) is very difficult especially for $p < 1$. It is an NP-Hard problem for $p = 0$. However, if all components except for the k^{th} one are fixed, then a problem can be solved by hard thresholding (for $p = 0$) or soft thresholding (for $p = 1$) of the marginal residuals $\mathbf{r}_k = \mathbf{s} - \sum_{l \neq k} \mathbf{\Phi}_l \mathbf{x}_l$ in $\mathbf{\Phi}_k$. The marginal residuals $\mathbf{r}_k$ contain potentially significant content about $\mathbf{y}_k$. MCA is a coarse-to-fine process in which the most salient contents of each component is calculated at each iteration. These estimates are then progressively refined as the threshold reduces.

4 Methods

In this section, the proposed vessel and exudate detection algorithm based on morphological component analysis and dictionary learning is discussed in detail. The proposed method is composed of three fundamental stages:

1) Preprocessing, this involves extracting the region of interest from the retinal image, removing the non-uniform illumination by a large mask median filter and then enhancing the contrast by local histogram equalization.
2) Obtaining vessels and exudates components of the input, using the learnt dictionaries and decomposition method based on BAMCA.
3) Postprocessing, Vessel and exudate segmentation which is applied to the corresponding separated components.

4.1 Preprocessing

Since the vessels and exudates have the highest contrast with the background in the green plane of color fundus image, this plane is chosen to implement the proposed method. To accelerate further processing stages, a *region of interest* (ROI) located at the center of the image and surrounded by dark background pixels is detected. To obtain ROI, a mask is applied to the retinal image and the retinal image is cropped with the mask. To generate the mask, Otsu thresholding algorithm [80] is applied to the green plane of the retinal image then morphological operations are used to remove missed labeled pixels that are generated on the mask. To accelerate next processing stages, the cropped retinal image is downsized to 512 × 512 by bicubic interpolation method. The background intensity variations in the fundus image can be eliminated by estimating the background image $\mathbf{I}_B$ with a median filter of size 30 and subtracting it from the original green plane image $\mathbf{I}_G$ as follows:

$$\mathbf{I}_{Enh}(i.j) = \mathbf{I}_G(i.j) - \mathbf{I}_B(i.j) \tag{5}$$

where $\mathbf{I}_{Enh}$ is the enhanced retinal image. Finally the values of $\mathbf{I}_{Enh}$ are normalized to the range of 0 to 1. Furthermore, to improve locally the contrast of the image the Contrast-Limited Adaptive Histogram Equalization (CLAHE) [81] is applied to the image $\mathbf{I}_{Enh}$.

4.2 Exudate and vessels separation

The blood vessels and exudate lesions appear as curved-like and deposits dot-like with sharp borders. Therefore, these components are morphologically distinct and can be separated using appropriately adapted MCA. To properly separate the components of the retinal image, it is crucial to construct two appropriate dictionaries; each of which sparsely represents one of the morphological components corresponding to vessels and exudates. Traditionally, MCA is performed using fix dictionaries obtained from known transforms such as DCT, contourlet or shearlet. The complexity of the retinal image contents makes component separation with known transforms difficult. In order to improve the representation which more tightly fitted to the morphological components, we utilize a modified dictionary learning algorithm. In the following subsection, the modified dictionary learning algorithm is described.

4.2.1 Dictionary learning for vessel and exudate

In this paper, two distinct dictionaries $\mathbf{\Phi}_v$ and $\mathbf{\Phi}_e$ corresponding to vessel and exudate parts are learned from training images (see Fig. 1). The training images are selected randomly from the vessel and exudate lesion datasets. Similar to many sparse representation-based methods, each image is divided into N overlapping vectorized patches $\mathbf{s}^{\mathrm{i}} \in R^{M\times 1}$ for $i = 1. \ldots . N$. Each vectorized patch is then centered by subtracting the mean value of patch pixels. Using the training samples $\mathbf{S} = [\mathbf{s}^1. \mathbf{s}^2. \ldots . \mathbf{s}^N]$, the dictionary $\mathbf{\Phi} \in R^{M\times L}$ with L atoms (each column of the dictionary is called an atom) is learned as:

$$\{\mathbf{\Phi}. \mathbf{X}\} = \underset{\mathbf{\Phi}.\mathbf{X}}{\operatorname{argmin}} \ \|\mathbf{S} - \mathbf{\Phi}\mathbf{X}\|_{\mathrm{F}}^2 \quad \text{s.t. } \|\mathbf{X}\|_0 < T_0 \tag{6}$$

where $\mathbf{X} = [\mathbf{x}^1.\mathbf{x}^2.\ldots.\mathbf{x}^N]$ is the sparse coefficients matrix for the patches of $\mathbf{S}$ and T_0 controls the sparsity level. This model is used to learn vessel ($\boldsymbol{\Phi}_v$) and exudate ($\boldsymbol{\Phi}_e$) dictionaries.

K-SVD algorithm solves problem (6) using an alternate optimization on $\boldsymbol{\Phi}$ and $\mathbf{X}$. In the spare coding stage, $\boldsymbol{\Phi}$ is kept constant while $\mathbf{X}$ is obtained as optimal coefficients typically implemented using greedy orthogonal matching pursuit (OMP) [82] or gradient descent based basis pursuit (BP) [83]. The search for a better dictionary, dictionary update stage, is then performed column-wise using singular value decomposition (SVD).

In order to adapt K-SVD algorithm to generate vessel and exudate dictionaries for retinal images two slight but salient changes have been done in this paper. The first change is applied to the dictionary update stage in K-SVD. More specifically, assuming the coefficient matrix $\mathbf{X}$ is constants, the dictionary update stage in K-SVD algorithm is performed as:

$$\{\boldsymbol{\Phi}\} = \underset{\boldsymbol{\Phi}}{\operatorname{argmin}} \ \|\mathbf{S} - \boldsymbol{\Phi}\mathbf{X}\|_{\mathrm{F}}^2 \tag{7}$$

In this process, one column $\boldsymbol{\varphi}^t$ of the dictionary (i.e. one atom) is isolated from the others and Frobenius norm is rewritten as:

$$\|\mathbf{S} - \boldsymbol{\Phi}\mathbf{X}\|_{\mathrm{F}}^2 = \left\|\mathbf{S} - \sum_{j=1}^{L} \boldsymbol{\varphi}^j \mathbf{x}_j\right\|_{\mathrm{F}}^2 = \left\|\left(\mathbf{S} - \sum_{j\neq t} \boldsymbol{\varphi}^j \mathbf{x}_j\right) - \boldsymbol{\varphi}^t \mathbf{x}_t\right\|_{\mathrm{F}}^2 = \|\mathbf{E}^t - \boldsymbol{\varphi}^t \mathbf{x}_t\|_{\mathrm{F}}^2 \tag{8}$$

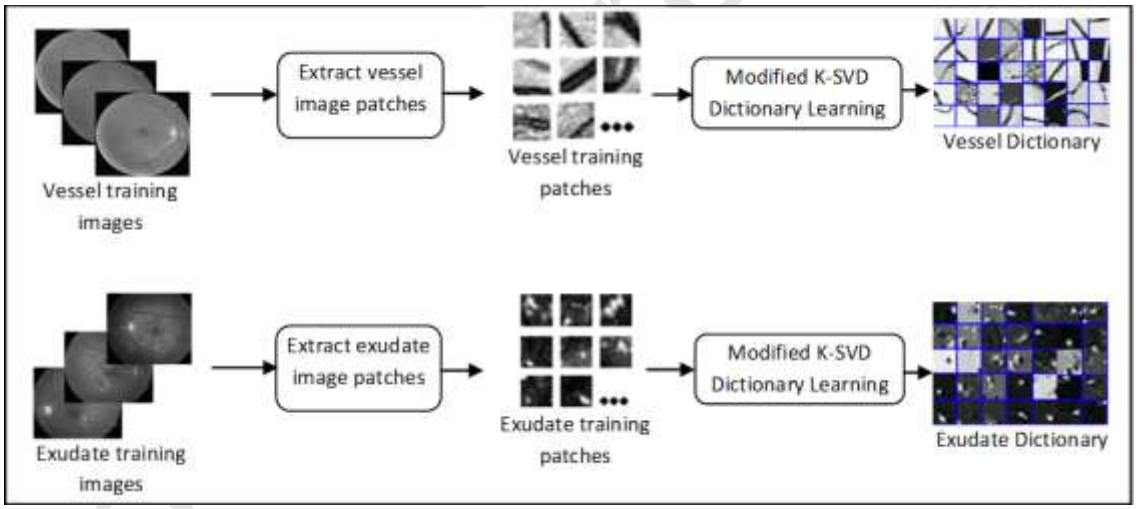

Fig. 1 Schematic representation of the dictionary learning method

where $\mathbf{x}_j$ is j^{th} row in the sparse coefficients matrix $\mathbf{X}$ and $\mathbf{E}^t = \left(\mathbf{S} - \sum_{j\neq t} \boldsymbol{\varphi}^j \mathbf{x}_j\right)$ is the error matrix. Therefore, the optimal solution for $\boldsymbol{\varphi}^t$ is obtained by minimizing the objective function given in Eq. (8). Let $(\mathbf{E}^t)_{\mathbf{R}}$ be obtained by choosing the columns of $\mathbf{E}^t$ that correspond to the samples which use atom $\boldsymbol{\varphi}^t$. The rank-one approximation of $(\mathbf{E}^t)_{\mathbf{R}}$ using SVD yields the atom $\boldsymbol{\varphi}^t$ and its corresponding coefficients. This process is repeated until all atoms are updated.

As noted earlier, the target source components, vessels and exudates, do not exist separately and in retinal images they are accompanied by noisy background. Therefore, as all sources are presented in the

samples, training the dictionaries is not straightforward. To tackle this issue, we construct the map matrix $\mathbf{G} = [\mathbf{g}^1.\mathbf{g}^2.\ldots.\mathbf{g}^N]$ where $\mathbf{g}^i$ corresponds to the binary map of vessel or exudate pixels of the patch $\mathbf{s}^i$ which is input to the algorithm for training samples as the ground truth. Using this matrix we can force the dictionaries to train only on the foreground which contain the main components of the retinal image. By discarding the complex and noisy background, the learning process is accelerated and enhanced. To do this, the error matrix $\mathbf{E}^t$ is changed to $\mathbf{E}^{*t}$ according to:

$$\mathbf{E}^{*t} = \mathbf{E}^t.\mathbf{G} = (\mathbf{S} - \sum_{j \neq t} \boldsymbol{\varphi}^j \mathbf{x}_j).\mathbf{G} \tag{9}$$

where the symbol "." represents the entry-wise product of matrices. In fact, the background pixels are ignored as they are multiplied by zeros in the corresponding map matrix $\mathbf{G}$. Therefore, the dictionary learning is modified to use a gated error $\mathbf{E}^{*t}$ defined as Eq. (9). Please refer to Algorithm 1 for more detail.

The second improvement is applied in dictionary initialization. The initialization of the dictionary is very important for the success of the dictionary learning algorithm. The underlying optimization problem is non-convex and may hence converge to suboptimal solutions. On the other hand, due to the computational cost associated with dictionary learning procedure, random re-initialization is practically inefficient. Therefore, a smart initialization is proposed in this paper. To initialize vessel and exudate dictionaries, patches with at least 10% of their pixels marked as vessel or exudate in the ground truth maps are selected as atoms of the corresponding dictionaries. These atoms are normalized to have unit l^2-norm. Moreover, in the initialization, mutual coherence between atoms in different dictionaries, measured as their inner product of two atoms, is used to remove similar atoms from the both dictionaries. This improves the discrimination capability of the two dictionaries.

Algorithm 1: The modified K-SVD dictionary learning algorithm

1. **Parameters:** $\mathbf{S} = [\mathbf{s}^1.\mathbf{s}^2.\ldots.\mathbf{s}^N]$ includes all image patches. $\mathbf{G} = [\mathbf{g}^1.\mathbf{g}^2.\ldots.\mathbf{g}^N]$ is the ground truth map matrix includes all binary vessel or exudate maps. $\mathbf{X} = [\mathbf{x}^1.\mathbf{x}^2.\ldots.\mathbf{x}^N]$ is the sparse coefficients matrix. T_0 controls the sparsity level.
2. **Initialize:** Set the dictionary $\boldsymbol{\Phi}^{(0)} \in \mathrm{R}^{\mathrm{M}\times\mathrm{L}}$ with unit l^2-norm columns. Set $J = 1$.
3. **Perform until convergence:**

   Update the coefficients: Use OMP algorithm to compute the coefficients matrix $\mathbf{X}$ by solving:

   $$\min_{\mathbf{X}} \|\mathbf{S} - \boldsymbol{\Phi}\mathbf{X}\|_2^2 \quad \text{s.t. } \|\mathbf{X}\|_0 < T_0$$

   Update the dictionary: Each column $k = 1.\ldots.L$ of the dictionary $\boldsymbol{\Phi}^{(J-1)}$ updated as:

   – Compute the residual matrix $\mathbf{E}^{*t}$:

   $$\mathbf{E}^{*t} = (\mathbf{S} - \sum_{j \neq t} \boldsymbol{\varphi}^j \mathbf{x}_j).\mathbf{G}$$

   – Obtain $(\mathbf{E}^{*t})_{\mathrm{R}}$ by choosing the columns of $\mathbf{E}^{*t}$ that correspond to the samples which use atom $\boldsymbol{\varphi}^t$.
   – Apply SVD to $(\mathbf{E}^{*t})_{\mathrm{R}} = \mathbf{U}\boldsymbol{\Delta}\mathbf{V}^{\mathbf{T}}$. Set the updated atom $\widehat{\boldsymbol{\varphi}}^t$ to the first column of $\mathbf{U}$ and the corresponding coefficients $\hat{\mathbf{x}}_t$ to the first column of $\mathbf{V}$ multiplied by $\boldsymbol{\Delta}(1.1)$.
   Set $J = J + 1$
4. **Output:** Dictionary $\boldsymbol{\Phi}$.

4.2.2 BAMCA method for exudate and vessel separation

As discussed in the previous subsection, the off-line learnt dictionaries $[\boldsymbol{\Phi}_v.\boldsymbol{\Phi}_e]$, provide sparse representation for vessel and exudate components of the retinal image. In this section, BAMCA method

(refer to Algorithm 2) which is used to separate vessels from exudate lesions based on these learnt dictionaries is described.

In Algorithm 2, $\mathbf{I}_v$ and $\mathbf{I}_e$ are the current vessel and exudate parts that are initialized to zero. At each iteration, the residual $\mathbf{I}_r = \mathbf{I} - \mathbf{I}_v - \mathbf{I}_e$ is obtained and the coefficients of the residual over vessel and exudate dictionaries are calculated. To obtain the coefficients matrix $\mathbf{X}^{res}$ for the residual image, patches are extracted from the residual image. Then for each vectorized patch, the coefficient vector $\mathbf{x}^{res}$ is calculated using BP problem (for p = 1) given in Eq. (4). The coefficients matrix $\mathbf{X}^{res}$ is constructed by concatenating all coefficients vectors as $\mathbf{X}^{res} = [\mathbf{x}^{\mathbf{res}1}.\mathbf{x}^{\mathbf{res}2}.\ldots.\mathbf{x}^{\mathbf{res}N}]$ where N is the total number of patches. These coefficients determine the value of the threshold. The method that the threshold is determined can affect the quality of the separation.

In this paper, the adaptive thresholding strategy, namely, mean of maximum (MOM) [84] has been selected. The threshold ξ is set to the mean of the largest values of the residual coefficients over vessel and exudate dictionaries. If the largest coefficient corresponds to the vessel dictionary, i.e. vessel dictionary wins, the vessel part $\mathbf{I}_v$ is updated while the looser exudate part $\mathbf{I}_e$ remains fixed, and vice versa. In this update process, negligible coefficients of the winner dictionary are discarded to keep the representation sparse. However, to compensate for the lack of individually insignificant coefficients which overall may contribute significantly to the representation of the input image patch, the survived coefficients are re-estimated through least squares.

More formally, let $\mathbf{\Phi}_v^{ind}$ and $\mathbf{x}_v^{i\ ind}$ be the sub-matrices that include the survived atoms and coefficients then to obtain the new coefficients $\hat{\mathbf{x}}_v^i$, the following optimization problem is solved using nonlinear least squares:

$$\hat{\mathbf{x}}_v^i = \underset{\mathbf{x}_v^i}{\operatorname{argmin}} \left\| \mathbf{s}_v^i - \mathbf{\Phi}_v^{ind} \mathbf{x}_v^{i\ ind} \right\|_2^2 \tag{10}$$

where $\mathbf{s}_v^i$ is i^{th} patch extracted from $\mathbf{I}_{rv}$ (the sum of the residual and vessel part image is $\mathbf{I}_{rv}$). Then the image patch is reconstructed with the new coefficients and finally all patches are averaged to reconstruct the vessel part image $\mathbf{I}_v$.

Algorithm 2: The proposed BAMCA decomposition method

1. **Parameters:** The enhanced image $\mathbf{I}_{Enh}$, the vessel and exudate dictionaries $\mathbf{\Phi} = [\mathbf{\Phi}_v.\mathbf{\Phi}_e]$, number of iterations N_{iter}, stopping threshold ξ_{min} and the regularization parameter λ.
2. **Initialize:** Let set $\mathbf{I} = \mathbf{I}_{Enh}$, the matrix **RFM = {1}** and **UFM = {0}**. Initial solution $\mathbf{I}_v = 0$, $\mathbf{I}_e = 0$, the residual image of the previous iteration $\mathbf{I}_r^{prev} = 0$.
3. **Perform** N_{iter} **times:**
   Calculate the residual image $\mathbf{I}_r = \mathbf{I} - \mathbf{I}_v - \mathbf{I}_e$
   Obtain the coefficients $\mathbf{X}_v^{res}$ over the dictionary $\mathbf{\Phi}_v$ for $\mathbf{I}_r$ using the sub-algorithm 2.1.
   Obtain the coefficients $\mathbf{X}_e^{res}$ over the dictionary $\mathbf{\Phi}_e$ for $\mathbf{I}_r$ using the sub-algorithm 2.1.
   Calculate the threshold: $\xi = \frac{1}{2}(\|\mathbf{X}_v^{res}\|_\infty + \|\mathbf{X}_e^{res}\|_\infty)$
   If $(\xi < \xi_{min})$ finalized the algorithm. Else continue.
   If $(\|\mathbf{X}_e^{res}\|_\infty < \|\mathbf{X}_v^{res}\|_\infty)$
   Update $\mathbf{I}_v$ assuming $\mathbf{I}_e$ is fixed:
   – Calculate the image $\mathbf{I}_{rv} = \mathbf{I}_r + \mathbf{I}_v$.
   – Obtain the coefficients $\mathbf{X}_v$ over the dictionary $\mathbf{\Phi}_v$ for image $\mathbf{I}_{rv}$ using sub-algorithm 2.2.
   – Obtain $ind = \{j | 1 \le j \le L\ \mathbf{x}_v^i(j) > \xi\}$ for each patch $\mathbf{s}_v^i\ \ i = 1.\ldots.N$.
   – Construct the sub-matrix $\mathbf{\Phi}_v^{ind}$ that includes the selected atoms for each patch.
   – Obtain the new coefficients $\hat{\mathbf{x}}_v^i$ using Eq. (10) and reconstruct the patch as $\hat{\mathbf{s}}_v^i = \mathbf{\Phi}_v^{ind}\hat{\mathbf{x}}_v^i$.

– Average all overlapping patches $\hat{\mathbf{s}}_v^i$ to reconstruct $\mathbf{I}_v$.

Else

Update $\mathbf{I}_e$ assuming $\mathbf{I}_v$ is fixed:

– Calculate the image $\mathbf{I}_{re} = \mathbf{I}_r + \mathbf{I}_e$.

– Obtain the coefficients $\mathbf{X}_e$ over the dictionary $\mathbf{\Phi}_e$ for image $\mathbf{I}_{re}$ using sub-algorithm 2.2.

– Obtain $ind = \{j | \, 1 \le j \le L \;\; \mathbf{x}_e^i(j) > \xi\}$ for each patch $\mathbf{s}_e^i \;\; i = 1. \ldots . N$.

– Construct the sub-matrix $\mathbf{\Phi}_e^{ind}$ that includes the selected atoms for each patch.

– Obtain the new coefficients $\hat{\mathbf{x}}_e^i$ using Eq. (10) and reconstruct the patch as $\hat{\mathbf{s}}_e^i = \mathbf{\Phi}_e^{ind} \hat{\mathbf{x}}_e^i$.

– Average all overlapping patches $\hat{\mathbf{s}}_e^i$ to reconstruct $\mathbf{I}_e$.

Set $\mathbf{I}_r^{prev} = \mathbf{I}_r$

4. **Output:** Morphological components $\mathbf{I}_v$ and $\mathbf{I}_e$

MCA is a coarse-to-fine iterative algorithm, as it progresses the variance of the residual is likely to decrease and the resulting components converge. Therefore, a stopping threshold ξ_{min} is used to end the main loop when further iteration does not change the results significantly. Please refer to Algorithm 2 for more detail. The schematic representation of the proposed decomposition method based on BAMCA method has been shown in Fig. 2 (a). After separating, one possible approach to evaluate the quality of vessel or exudate components quantitatively, is analyzing each part to extract the binary vessel or exudate maps, see Fig. 2 (b). To do this, we use our previous works on vessel and exudate segmentation which are recently developed [6], [7]. The vessel segmentation algorithm is based on Morlet wavelet transform and adaptive thresholding. Mathematical morphologies and dynamic thresholding are used in the exudate segmentation algorithm. The detail of the segmentation algorithms has been provided in [6], [7].

To enhance the computational efficiency of the proposed BAMCA method some improvements have been suggested. These improvements are shown in the sub-algorithm 2.1 and 2.2 and will be described in detail in the following subsection.

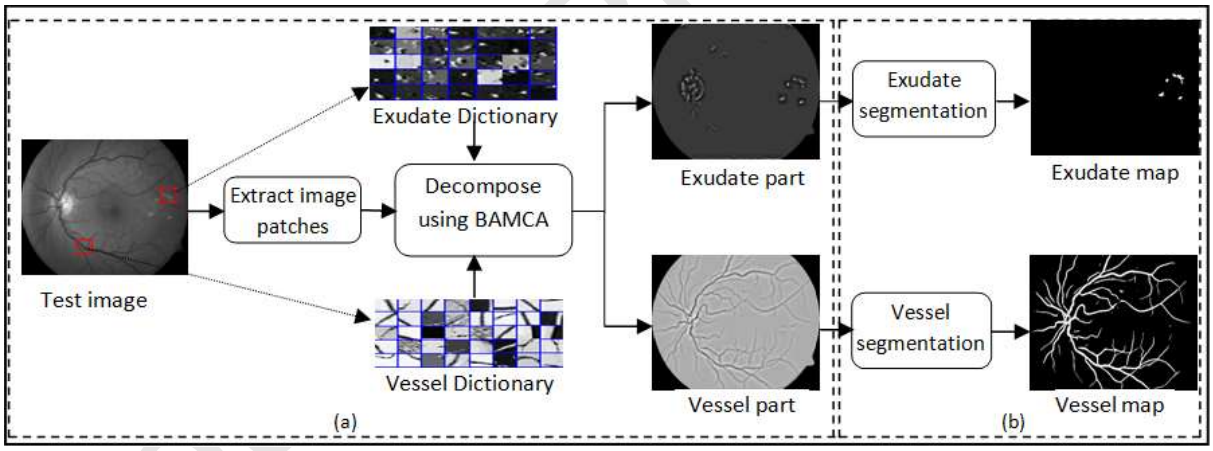

Fig. 2 Schematic representation of the proposed method (a) decomposition method based on BAMCA method; (b) vessel and exudate segmentation

4.2.3 Improved BAMCA method for separation

In MCA algorithm, the number of necessary iterations is important but difficult to estimate. There is no general method to adjust it. Using a large number is computationally expensive, whereas, a poor separation may be resulted if it is set too small. According to our experiments on separation of retinal image components, the adaptive thresholding based on MOM leads to the best quality. However, number of iterations may easily reach to a hundred or more and hence, the decomposition process get inefficient and slow. Therefore, in the following, we also suggest some minor but crucial improvements to considerably increase the efficiency of our method.

Since the energy of the residual is decreased along iterations, processing the patches which are already reconstructed in the previous iterations for few times would be useless since usually they are not left with any salient content. We name these patches as useless patches and omit them from the competition in the next iterations. If, the maximum value of coefficients of a patch is below the threshold, ξ_{min}, it is marked as a useless patch and its corresponding coefficients will not be recalculated in the next iterations till the end of the algorithm, leading to noticeable reduction in run time and improvement in the computational efficiency of BAMCA method.

Furthermore, in the global competition phase in each iteration, only few patches get seriously involved, and values of the coefficients in many others, regardless of which dictionary is considered, remain well below the current threshold, ξ. Therefore, such patches are not handed over to any specific dictionary and remain unchanged during the current iteration. This means it is not necessary to recalculate their coefficients in the next iteration. However, since the patches overlap, we should take care of the regions which are shared with other changing patches. In fact, only the completely unchanged patches are omitted from the representation phase obtained by BP problem for just the next iteration. The representations for other patches are updated as usual if the residual norm difference between the last two iterations is greater than another threshold ξ_{diff}; otherwise they are also skipped over in the next iteration. All these improvements are considered in sub-algorithm 2.1 and 2.2, and combined together, they save up to 90% of the normal run time of the algorithm.

Sub-algorithm 2.1: Improved residual coefficients calculation algorithm

1. **Parameters:** The current residual image $\mathbf{I}_r$ and previous one $\mathbf{I}_r^{prev}$, the dictionary $\mathbf{\Phi}_d$ where $d = v$ or e, the residual coefficients matrix $\mathbf{X}_d^{res}$, the difference threshold ξ_{diff},the threshold ξ_{min}. Reconstructive flag matrix **RFM**. Useless flag matrix **UFM**.
2. **Perform:**
   Extract all patches $\mathbf{r}^i \; for \; i = 1. \ldots . N$ from the current residual image $\mathbf{I}_r$.
   Extract all patches $\mathbf{r}^{i\ prev} \; for \; i = 1. \ldots . N$ from the previous residual image $\mathbf{I}_r^{prev}$.
3. **Perform** *N* **times:**
   Calculate $= \|\mathbf{r}^i\|_2 - \|\mathbf{r}^{i\ prev}\|_2$.
   If ($diff < \xi_{diff}$**)**
      Set to zero, the element *i* corresponding to the patch $\mathbf{r}^i$ in **RFM** matrix.
   Else
      If (RFM(*i*)=1 and UFM(*i*)=0)
         Update coefficients $\mathbf{x}^{i\ res}$ for patch $\mathbf{r}^i$ over the dictionary $\mathbf{\Phi}_d$ using Eq. (4).
         If $\|\mathbf{x}^{i\ res}\|_\infty < \xi_{min}$
            Set to one, the element *i* corresponding to the patch $\mathbf{r}^i$ in **UFM** matrix.
4. **Output:** The coefficients $\mathbf{X}_d^{res}$, the matrix **RFM** and the matrix **UFM**

Sub-algorithm 2.2: Improved reconstruction algorithm

1. **Parameters:** The image $\mathbf{I}_{rd}$ where $d = v$ or e, the dictionary $\mathbf{\Phi}_d$, the threshold ξ. The coefficients matrix $\mathbf{X}_d$. Reconstructive flag matrix **RFM**. Useless flag matrix **UFM**.
2. **Perform:**
   Extract all patches $\mathbf{s}^i \; for \; i = 1. \ldots . N$ from the image $\mathbf{I}_{rd}$.
3. **Perform** *N* **times:**
   If (RFM(*i*)=1 and UFM(*i*)=0)
      Update the coefficients $\mathbf{x}^i$ for patch $\mathbf{s}^i$ over the dictionary $\mathbf{\Phi}_d$ using Eq. (4).
   If ($\|\mathbf{x}^i\|_\infty > \xi$)
      Set to ones, the elements *i* and its neighbors in the matrix **RFM** for using in the next iteration.
   Else
      Set to zero, the element *i* in the matrix **RFM** for using in the next iteration.
4. **Output:** The coefficients $\mathbf{X}_d$ and the matrix **RFM**

5 Experimental results

5.1 Materials

To evaluate the vessel segmentation algorithm, two public datasets DRIVE [36] and STARE [23] which contain ground truth vessel maps are used. DRIVE dataset contains a total of 40 color fundus images divided into equal training and test set of images with size 584 × 565. Since a large number of patches are extracted from one image, only a few number of images are selected to train dictionaries. To learn the vessel dictionary, training patches are randomly extracted from four images of DRIVE training dataset. The performance of the proposed method is measured on the test images of DRIVE and STARE dataset which includes 20 color fundus images of size 605 × 700.

In the following, the performance of the exudate segmentation is assessed using DIRATEDB1 [85] and e-ophtha EX datasets[54]. The public dataset DiaretDB1 contains 89 retinal images with a resolution of 1500 × 1152 pixels. Randomly, four images of DIRATEDB1dataset are selected for training the dictionary and the remaining ones are used for the test phase. E-ophtha EX dataset which contains 47 images with four different resolutions, ranging from 1440 × 960 to 2544 × 1696 pixels, is also used to measure the performance of the proposed method.

5.2 Performance measures

The performance of the binary segmentation methods is usually quantitatively assessed based on three measures: Sensitivity, Specificity and Accuracy, which are defined as:

$$Sen = \frac{true\ positive}{true\ positive + false\ negative} \tag{11}$$

$$Spec = \frac{true\ negative}{false\ positive + true\ negative} \tag{12}$$

$$Acc = \frac{true\ positive + true\ negative}{true\ positive + true\ negative + false\ positive + false\ negative} \tag{13}$$

In vessel segmentation, these measures are evaluated at pixel level as the output vessel map is a single connected component. On the other hand, in detection of lesions it is quite natural to evaluate the screening results at the image level based on presence or absence of lesions in each image. In other words, the segmentation result for an image is considered as true positive (or true negative) if the input image contains (doesn't contain) exudates according to both the segmentation method and the ground truth. Based on this definition, the rest of indicators are similarly calculated. However, in clinical usages further than screening where localization of separated lesion regions is desired, more exact assessment can be obtained by calculating the above measures at lesion level. At this level, the calculation of true and false positives and negatives is carried on based on the percentage of overlapped pixels of each lesion region in the output map and the ground truth. In fact, when a minimum amount of overlap is detected[1], then all of the pixels corresponding to that lesion are counted as true positives and similarly for the rest of indicators, then the above measures are obtained; see [54] for more details.

Since, the threshold value used in the final stage of segmentation [6], [7] is affecting the aforementioned measures; we report the receiver operating characteristic (ROC) curve by plotting Sensitivity as the vertical axis versus (1-Specificity) as the horizontal axis when changing the threshold

[1] To provide comparable results, the same value suggested by Zhang et al. [54] is used here and the minimal overlap ratio is set to 0.2.

over its range. Area under ROC curve (AUC) summarizes each curve in a single number and the reported values in the tables are selected as points of ROC with approximately highest accuracy.

5.3 Parameter setting

In the proposed method, after preprocessing stage, vessel and exudate dictionaries are learnt using patches extracted from the training images. The patch size is set to 16×16 with sliding distance of 5 pixels to train a dictionary of 1024 atoms with four-fold redundancy. Using training patches, the maximal number of coefficients or the sparsity level T_0 in Eq.(6) is set to 10. In order to improve the efficiency of the learning dictionaries, patches which at least 10% of their pixels marked as vessel or exudate in the ground truth maps are considered as training patches. In addition, some of these patches which have low mutual coherence (less than 80%) are selected for the initialization of the dictionaries. The atoms of dictionaries are normalized to have unit l^2-norm. The parameters of BAMCA algorithm (Algorithm 2) are empirically set using numerous experiments on training images as follows: The number of iterations N_{iter} is set to 100 since further iterations does not seem to have significant effect on the results of separation; the regularization parameter λ is adjusted to 40% of the maximum image intensity and the value of the stopping threshold ξ_{min} is considered to be 10^{-4}. The threshold value ξ_{diff} was set to 0.08. The selected settings for different parameters in this paper may not be optimal. More careful cross validation may help to choose better values for the parameters and improve the results reported here.

5.4 Experiments

Comparison between different image separation algorithms is greatly dependent on the application and hence is done according to the considered target task [77]. In this paper, in addition to visual qualitative assessments, we want to quantitatively measure the performance of the proposed method in effectively separating diagnostically helpful components of the retinal image. Therefore, we devise four different experiments:

First, the decomposition results are shown on sample retinal images to visually inspect the separated components and judge their quality. Then, in the second and third experiments, results of vessel and exudate segmentation are quantitatively compared to some state-of-the-art segmentation algorithms. Finally, in the last part of this section, the results of two well-known and publicly available vessel segmentation algorithms are reported in two different scenarios as the forth experiment: when BAMCA is acting as preprocessing step and calls the segmentation algorithm on the obtained vessel part versus the usual case where the original retinal image is used as input.

5.4.1 Separation of vessel and exudate components in retinal image

The results of applying BAMCA method to seven sample abnormal retinal images[1] are illustrated in Fig. 3, where Fig. 3 (b) depicts the vessel parts and Fig. 3 (c) shows the obtained exudate components which are renormalized to completely span the available range of gray scales. As it can be seen, the presence of noisy background does not affect the performance of our separation algorithm; as such additional contents are sparsely represented by neither of vessel nor exudate dictionaries. Therefore, the exudate component is well separated from the vessel part in the shown examples. This is an important achievement, since the output of our system is supposed to be used visually by ophthalmologists to support clinical decision making. According to International Council of Ophthalmology, DR grading can be done based on location of exudate lesions with respect to the optic disk and fovea [86]. Moreover,

[1] Image number 8 from DRIVE and image numbers 3,44, 6, 67,14,16 from DIARETDB1

providing physicians with the lesion components of the retinal image, help them make decisions on type and duration of treatment, scheduling patients' arrival to the clinic and other necessary status checks.

The obtained components from the separation phase are then fed to the segmentation algorithms [6], [7] to obtain binary vessel and exudate maps which are depicted in Fig. 3 (d) and (e) respectively. As shown, the binary vessel maps extracted well even in the third and seventh images which suffer from low contrast. Interestingly, in the first image (image number 8 from Drive), the obtained vessel map is quite clean and does not have noticeable false positive pixels. Most of state-of-the-art vessel segmentation algorithms fail on this image by including exudate pixels in their output vessel map, see for example [5], [24], [31]. Since DRIVE contains mostly healthy retinal images, such failures are less noticed in the reported numerical results.

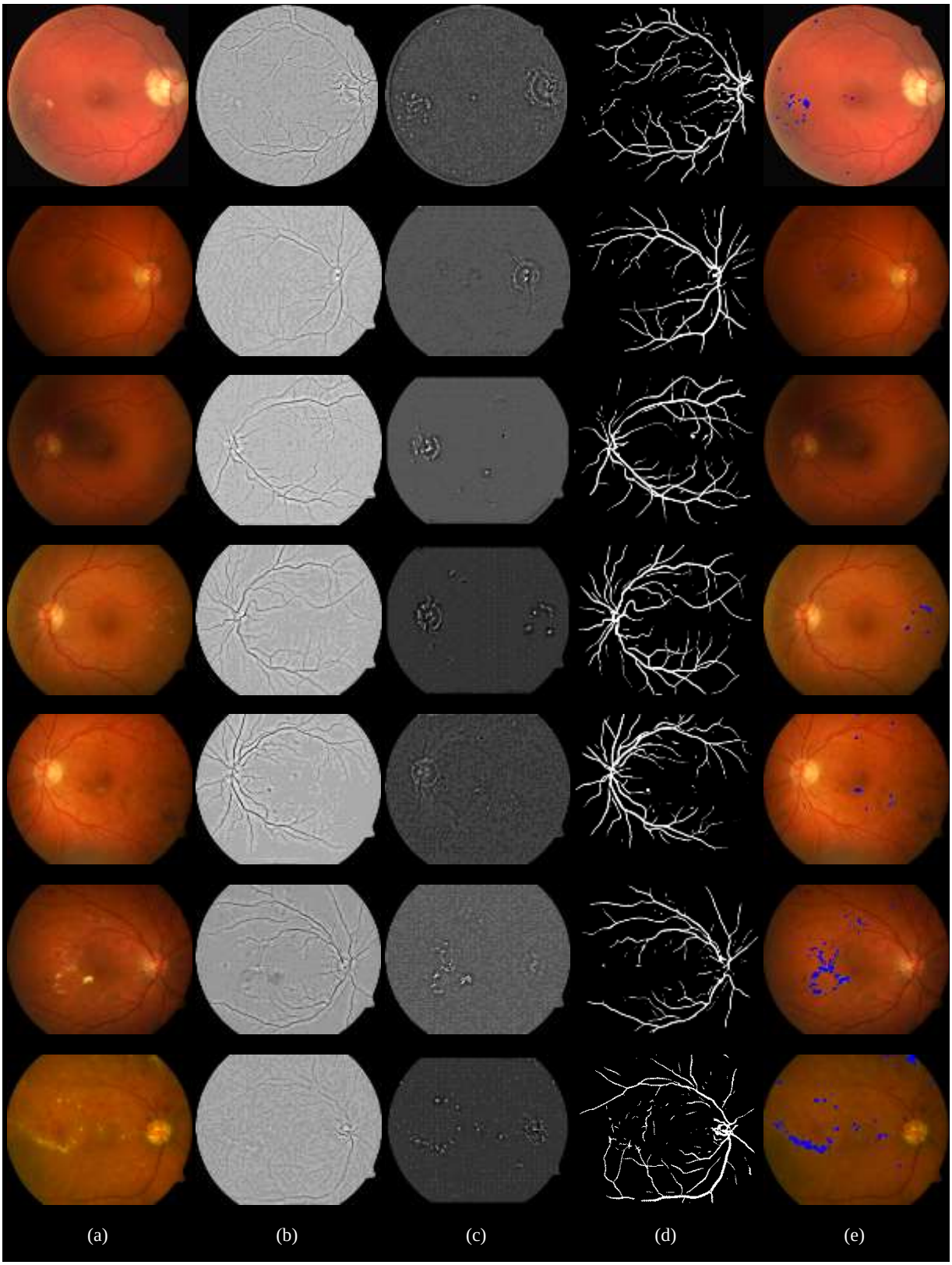

Fig. 3 Results of the vessel and exudate separation and segmentation algorithm on abnormal images (a) original retinal images; (b) vessel parts; (c) exudate parts; (d) vessel detection maps and (e) corresponding exudate detection maps

As mentioned earlier, the work presented by Imani et al. [6] is the only approach which separates the retinal image components. However, this method severely gets limited in the case of retinal images with proliferative DR. For better comparison, Fig. 4 shows the separation results obtained by Imani and our method for images with sever DR. As it can be seen, a major portion of exudates remains in the vessel component obtained by Imani (first row in Fig. 4 (c)) and some vessels with high tortuosity are also missed and appeared in the exudate lesion part (second row in Fig. 4 (e)) separated by Imani. Therefore, the capability of the proposed method shown in Fig. 4 (b) and (d) is superior in such pathological cases.

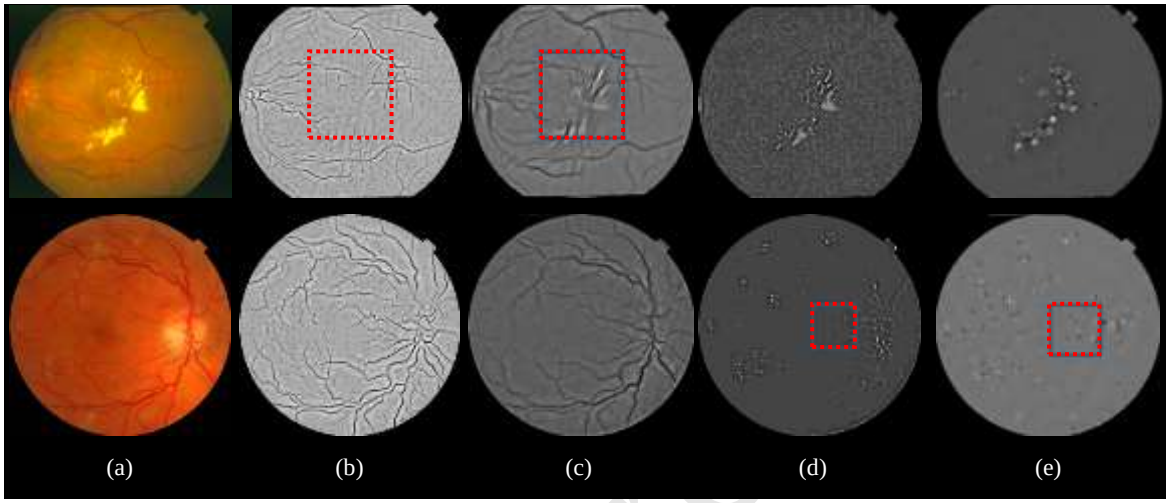

Fig. 4 Visual comparison of Imani et al. method [6] with the proposed BAMCA method: (a) original retinal images; vessel component separated by (b) BAMCA; (c) Imani et al. [6]; exudate component separated by (d) BAMCA; (e) Imani et al. [6]

5.4.2 Blood vessel segmentation

To quantitatively evaluate the quality of vessel component obtained by BAMCA, we use our previous work on vessel segmentation [6]. The extracted vessel component is input to the segmentation algorithm and the obtained vessel map is compared with the state-of-the-art vessel segmentation algorithms. The results in terms of ROC curves using DRIVE and STARE datasets are depicted in Fig. 5, which correspond to quite similar AUC values 0.9586 and 0.9523 respectively. Noticeably, the curves for the two different datasets are close together though STARE dataset contains much more abnormal images. This shows the consistency of the proposed method in working with normal and abnormal images which are visually very different.

Table 1 reports Sensitivity, Specificity and Accuracy obtained using the proposed method against some other state-of-the-art methods applied on both DRIVE and STARE datasets. Although the proposed method is a generative approach which delivers separated components of the retinal image and the binary maps considered in the segmentation experiments are its side products, yet the reported results are comparable with the methods originally designed for vessel segmentation or even better in most cases. Elbalaoui et al. [32] reports relatively high Sensitivity on STARE dataset although at the cost of lower Specificity and Accuracy. Since usually vessel pixels are roughly one quarter of the image, in adjusting the segmentation threshold loosing each percentage of Specificity may add around four percent to Sensitivity by encouraging the algorithm to denote unclear pixels as vessels. Hence, the reported higher Sensitivity in the third row of Table 1 is simply result of different parameter setting and does not bring

any advantage. Another common issue in traditional vessel segmentation methods is producing false positive vessel pixels around the optic disc boundary. To overcome this problem, Siva and Vasuki [43] eliminated this region from retinal images before vessel segmentation. Therefore, as the authors also mention in [43], their reported results in the fourth row of Table 1 are not directly comparable with others. The last three rows in Table 1 belong to state-of-the-art deep learning based approaches [69]–[71]. As it can be seen, the proposed method gains higher Sensitivity and Accuracy in comparison to CNN based approaches with the exception of Accuracy results reported by Li et al. [71] on STARE dataset. This can be caused by the fact that in our setup the algorithm has to learn from DRIVE and is tested on images of STARE while they use leave-one-out approach and train on STARE images which are considerably more similar to the left-out test case.

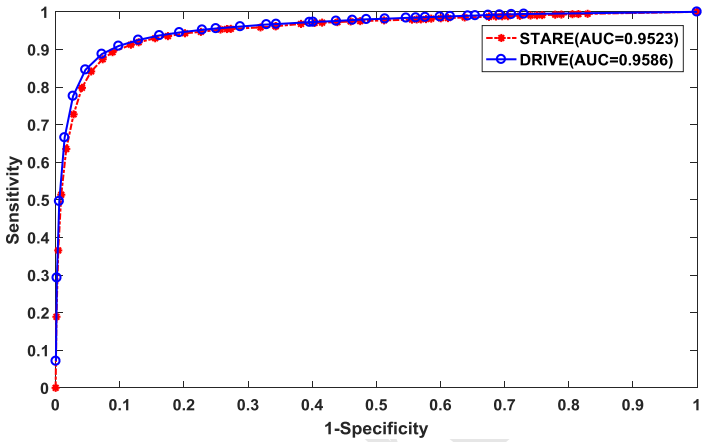

Fig. 5 ROC curve of the proposed method for vessel segmentation on DRIVE and STARE datasets

Table 1 Comparison results for vessel segmentation on DRIVE and STARE datasets

Method	DRIVE			STARE		
	Sen	Spec	Acc	Sen	Spec	Acc
Human observer	-	-	94.73	-	-	93.50
Nguyen et al.[31]	-	-	94.07	-	-	93.24
Elbalaoui et al. [32]	76.30	97.13	94.43	84.40*	94.76	93.26
Siva and Vasuki [43]**	93.99	98.37	98.08	93.60	98.96	95.94
Bankhead et al. [24]	70.27	97.17	93.71	-	-	-
Akram and Khan [26]	-	-	94.62	-	-	95.02
You et al. [37]	74	97	94	72	97	94
Delibasis et al. [18]	72.88	95.05	93.11	-	-	-
Lam et al. [42]	-	-	94.72	-	-	95.67
Miri and Mahloojifar [39]	-	-	94.58	-	-	-
Fraz et al. [40]	71.52	97.69	94.30	73.11	96.80	94.42
Imani et al. [6]	75.24	97.53	95.23	75.02	97.45	95.90
Zhang et al. [4]	58.09	98.97	-	73.91	99.52	-
Javidi et al. [5]	72.01	97.02	94.50	77.80	96.53	95.17
Melinscak et al. [69]	72.76	97.85	94.66	-	-	-
Maji et al. [70]	-	-	94.70	-	-	-
Li et al. [71]	75.69	98.16	95.27	77.26	98.44	96.28
Proposed method	**77.59**	**97.28**	**95.28**	**78.62**	**96.05**	**95.01**

*Higher Sensitivity is obtained at the cost of lower Specificity and Accuracy. At similar condition, our results would be Sensitivity=84.15, Specificity=94.46 and Accuracy=93.50.

**When optic disk is eliminated from retinal images before vessel segmentation.

To observe quality of vessel segmentation and obtain visual comparison of state-of-the-art, in Fig. 6, we show the binary vessel maps resulted from various methods on abnormal retinal images[1] which are intentionally selected to belong to different stages of DR. It is noticeable that vessel maps of our rivals, contain spurious components around optic disk and lesions; whereas simultaneous separation in the proposed method removes these false positives (marked as green circles in Fig. 6). Moreover, as can be seen, our method successfully extracts several thin vessels with more details.

[1] Image numbers 8,14 from DRIVE and image number 1from STARE

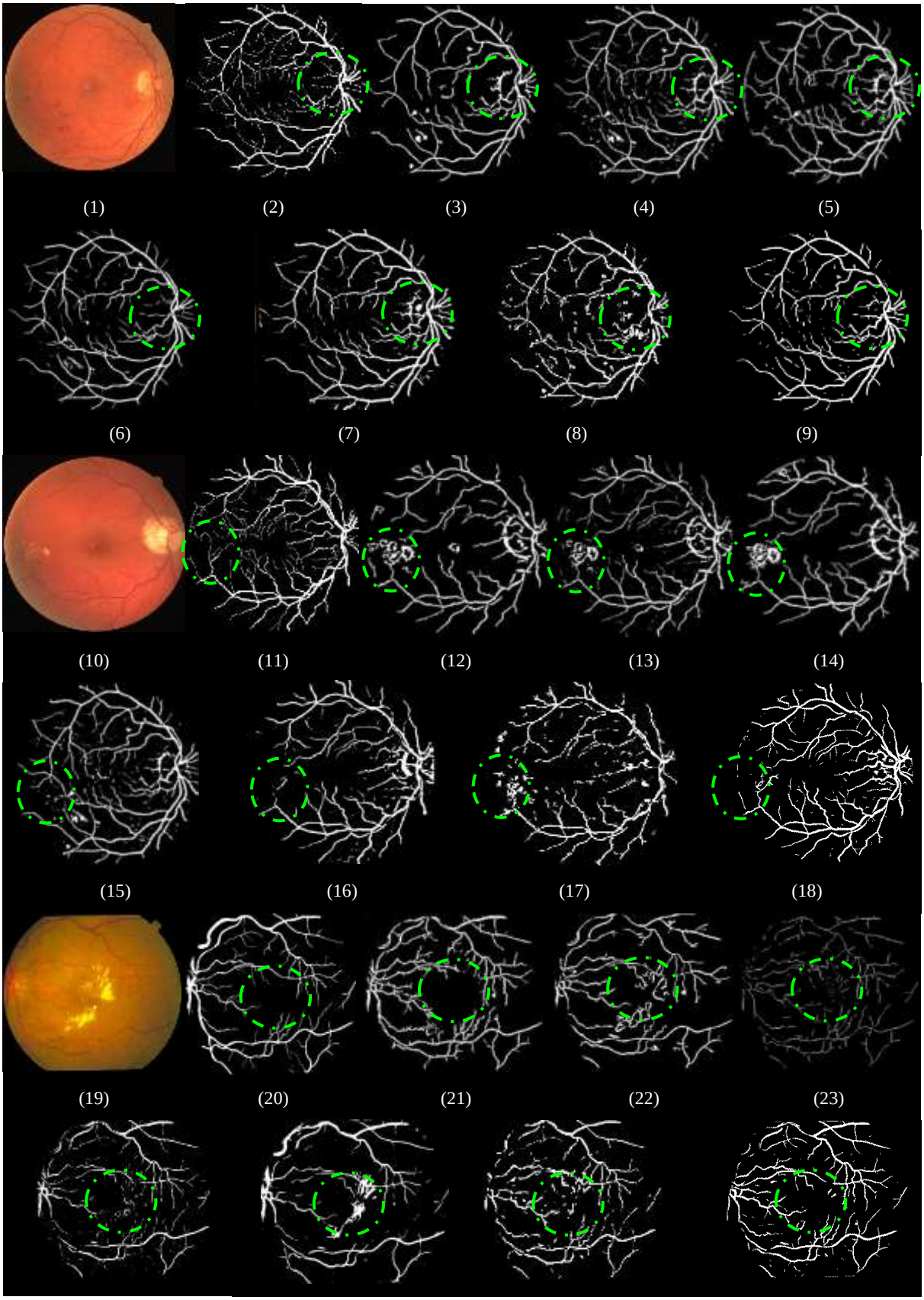

Fig. 6 Comparison results for different vessel segmentation algorithms on abnormal retinal images of DRIVE and STARE datasets: (1,10,19) RGB retinal images; vessel maps segmented (2,11,20) manually; (3,12) by Bankhead et al.[24] (4,13) by Nguyen et al.[31]; (5,14) Martinez et al.[28]; (6,15,24) Soares et al.[38]; (7,16,25) by Imani et al.[6] (8,17,26) by Javidi et al.[5] (9,18,27) by BAMCA method; (21) Wang et al.[25]; (22) Hoover et al.[23]; (23) Zhang et al.[4]

To visually assess vessel segmentation performance in different grading levels, Fig. 7 and Fig. 8 depict the obtained vessel maps for selected images from Kaggle [87] and IDRiD [88] datasets that are annotated with DR grading at 5 levels. As it can be seen, few lesions are detected as vessels, and the pathological lesions appearing with the progression of DR, do not have significant effect on the result of the vessel maps obtained by the proposed method. Advantageously, thin vessels around the lesions are also accurately extracted.

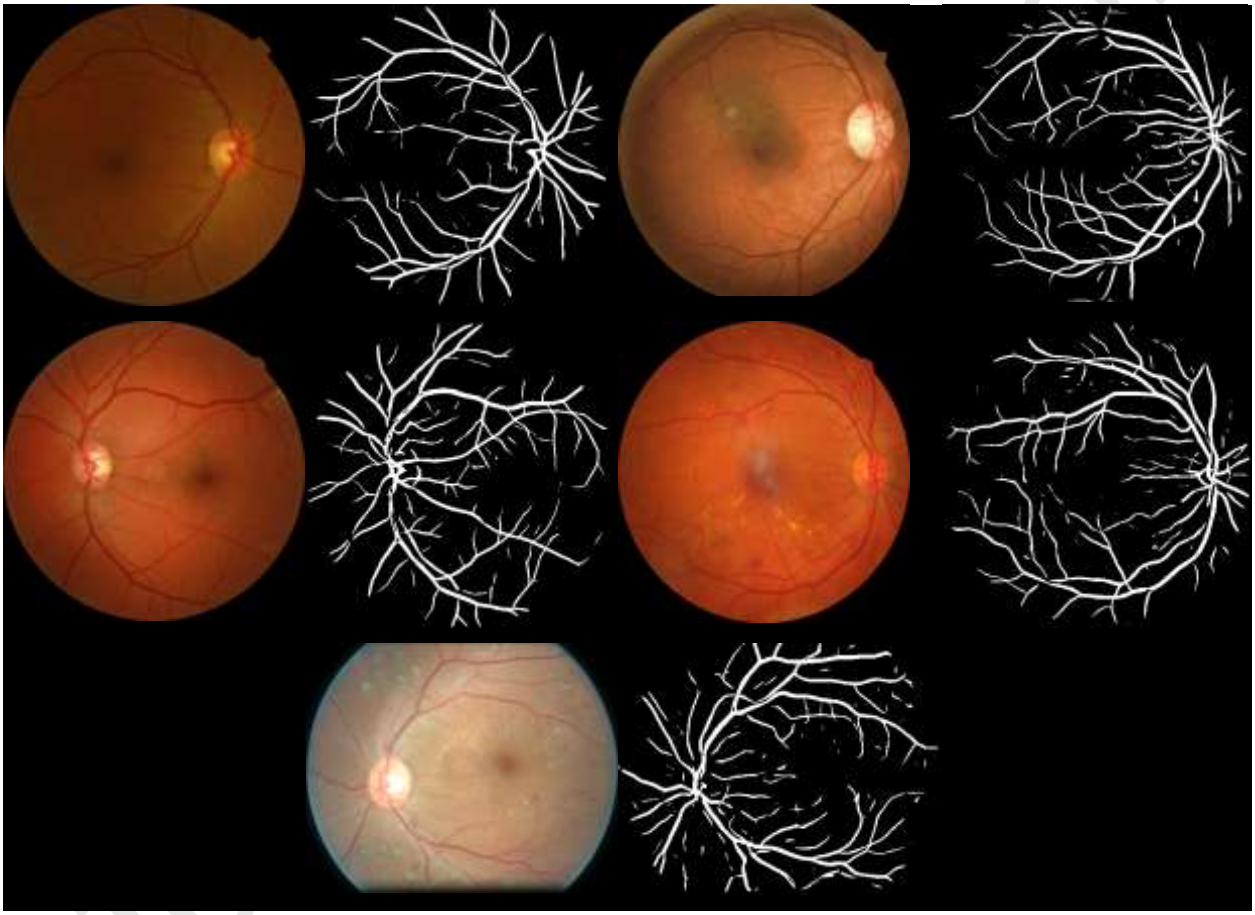

Fig. 7 The original retinal images and results of blood vessel segmentation of five severe stages of DR on Kaggle Database; from the top left to the bottom right: No DR (grade 0); Mild DR (grade 1); Moderate DR (grade 2); Severe DR (grade 3) and Proliferative DR (grade 4)

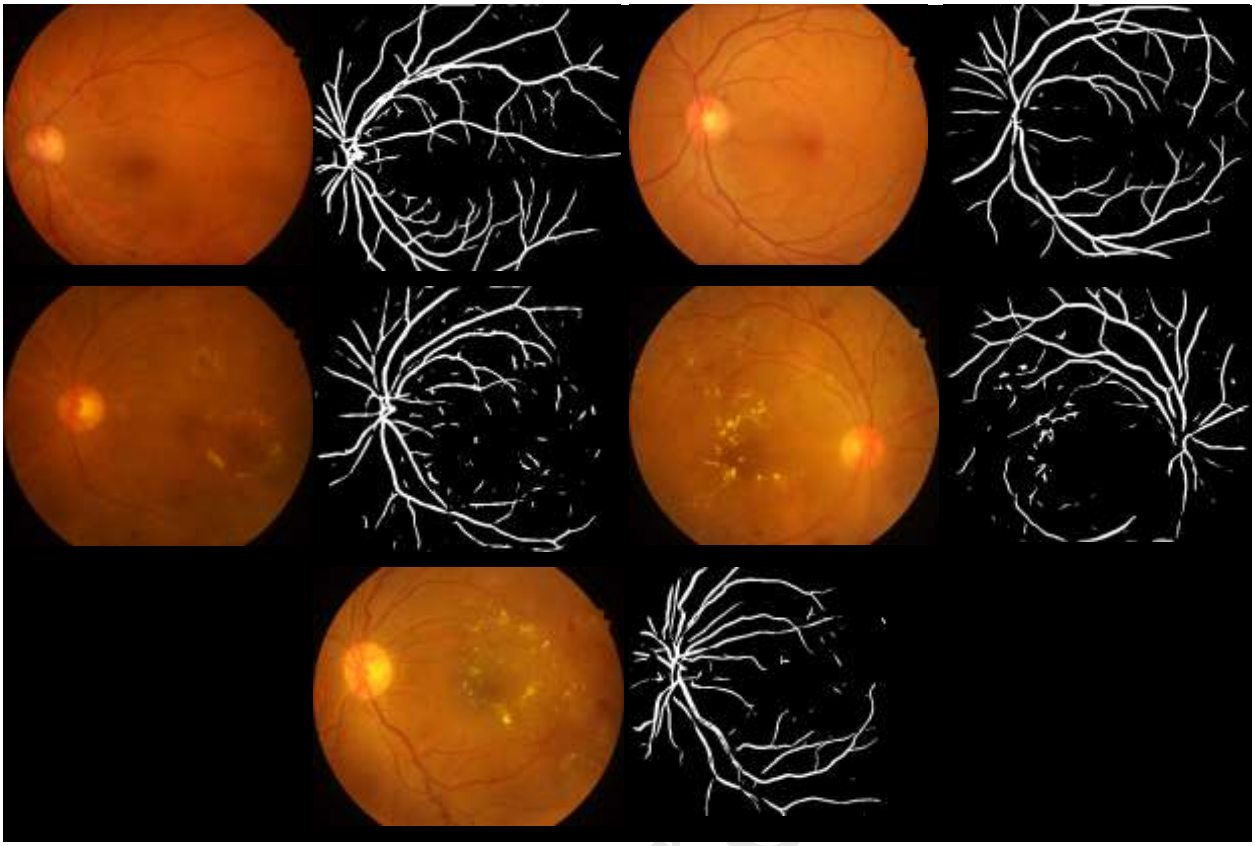

Fig. 8 The original retinal images and results of blood vessel segmentation of five severe stages of DR on IDRiD Database; from the top left to the bottom right: No DR (grade 0); Mild DR (grade 1); Moderate DR (grade 2); Severe DR (grade 3) and Proliferative DR (grade 4)

5.4.3 Exudate segmentation

In this section, the effectiveness of BAMCA in separation of exudate component is quantitatively evaluated both at exudate level and image level. For this purpose, the exudate segmentation method [7] is applied to the exudate component and the result is compared with the state-of-the-art exudate segmentation algorithms.

In exudate segmentation, non-exudate pixels by far dominate the retinal image. As a result, for typical segmentation algorithms Specificity approaches to one and ROC curve is highly compressed toward left. Therefore, to better compare performance of different methods, usually positive predictive value (PPV) is additionally reported. PPV is defined as:

$$PPV = \frac{true\ positive}{true\ positive + false\ positive} \tag{14}$$

Since ground truth images in e-ophtha EX dataset are carefully contoured by the expert, it is possible to evaluate a segmentation algorithm at lesion level as shown in Table 2. As can be seen, the results specially in terms of Sensitivity and PPV values are better than all methods even the most recent work proposed by Liu et al. [50]. On the other hand, as exudate maps in DIARETDB1 dataset contains rough annotations and they have not been precisely contoured, most state-of-the-art methods report their results at image level for this dataset. Hence, we similarly report image level Sensitivity, Specificity, and Accuracy values in Table 3. As it can be seen, our method performs equally well or even better.

Although it's not traditional to report free-response ROC (FROC) for exudate detection at lesion level but Quellec et al. [62] and Gondal et al. [75] report this curve to assess their performance. As mentioned, Quellec and Gondal methods correspond to deep learning approaches that has recently attracted considerable attention. To make a better comparison, FROC curves and the area under the FROC curve (AUC) are illustrated in Fig. 9. As it shown; our method outperforms their approaches so that for the same false positive rate, the proposed method yields higher Sensitivity. Furthermore, the image level ROC Curve of our exudate detection is compared against state-of-the-art in Fig. 10. Our approach performs superior to all traditional methods while Quellec's ensemble of deep CNNs surpasses it although with much smaller margin with respect to what it already lost in Fig. 9. Overall, this results suggest that we may obtain improved results if we invest more on post-processing which generate our image level outputs from the processed patches. Moreover, to visually compare the output exudate maps obtained by our method against Quellec et al. [62], Fig. 11 illustrates. As can be seen, our result outperforms Quellec's method by catching its missed lesion marked with green circle and reducing false positive clutters highlighted with red circle.

Table 2 Comparison of lesion level (region based evaluation with overlap ratio: 0.2) exudate detection on e-ophtha EX dataset

Method	AUC	Sen	Spec	PPV
Zhang et al. [54]	-	74	-	72
Walter et al. [51]	-	44	-	65
Welfer et al. [52]	-	79	-	55
Imani et. al. [7]	0.937	80.32	99.83	77.28
Liu et al. [50]	-	76	-	75
Proposed method	**0.9375**	**80.51**	**99.84**	**77.3**

Table 3 Comparison of image level exudate detection on DIARETDB1 dataset

Method	Sen	Spec	Acc
Walter et al. [51]	86	69	77
Welfer et al. [52]	100	0	48
Sopharak et al.[44]	100	14	64
Harangi and Hajdu [53]	92	68	82
Liu et al. [50]	83	75	79
Gondal et al. [75]	93.3	*	
Proposed method	**96**	**83**	**90**

* Specificity value 97.6% over all lesion types has been reported

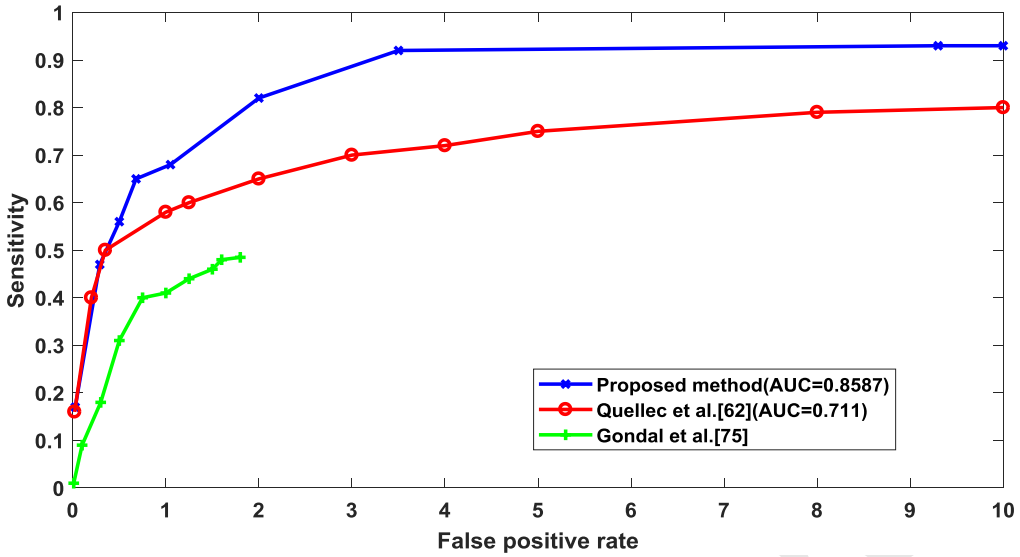

Fig. 9 Exudate detection performance at the lesion level on DIARETDB1 dataset

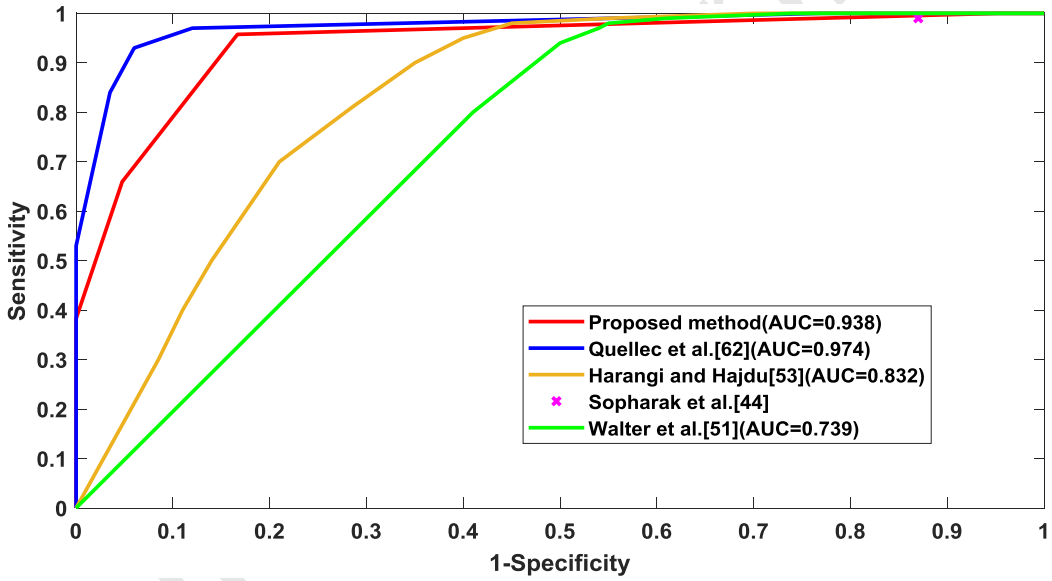

Fig. 10 ROC curve of image level exudate detection on DIARETDB1 dataset

Furthermore, at lesion level, the results in terms of ROC curves using DIARETDB1[1] and e-ophtha EX datasets are shown in Fig. 12, respectively corresponding to AUC values of 0.959 and 0.9375. As newer e-ophtha EX dataset contains trickier images, naturally our result is slightly worse on this dataset similar to other reported efforts. Corresponding visual comparison is given in Fig. 13. As can be seen, the proposed method can detect more true positive regions while keeping a low false negative rate.

[1] All exudate lesions in images of this dataset have been manually contoured for lesion level assessment.

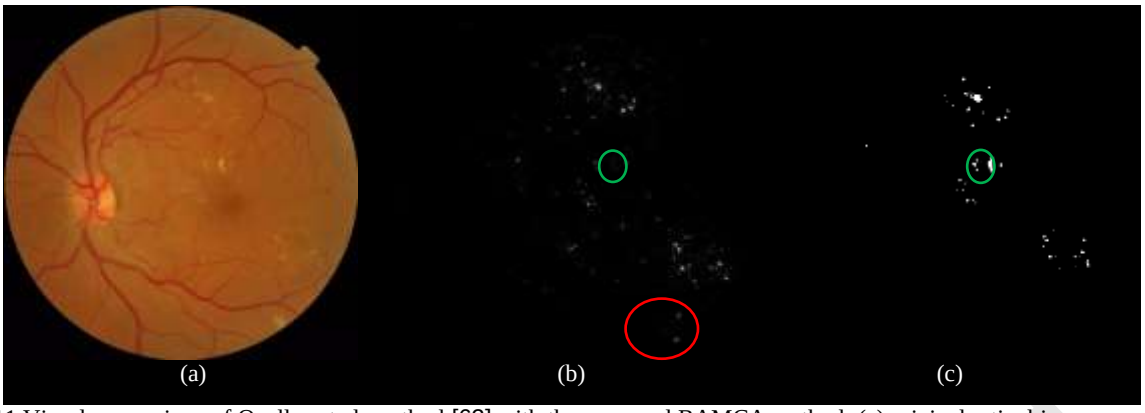

Fig. 11 Visual comparison of Quellec et al. method [62] with the proposed BAMCA method: (a) original retinal images; exudate map obtained by (b) Quellec et al [62] and (c) the proposed BAMCA method

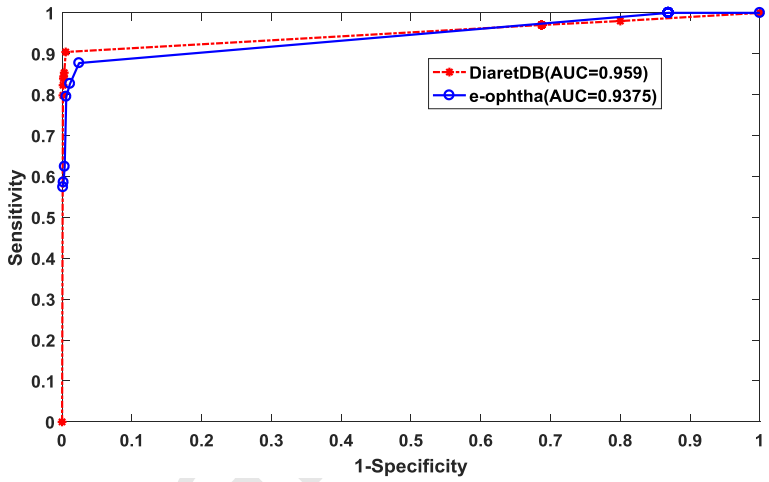

Fig. 12 ROC curve of the proposed method for lesion level exudate detection on DIARETDB1 and e-ophtha EX datasets

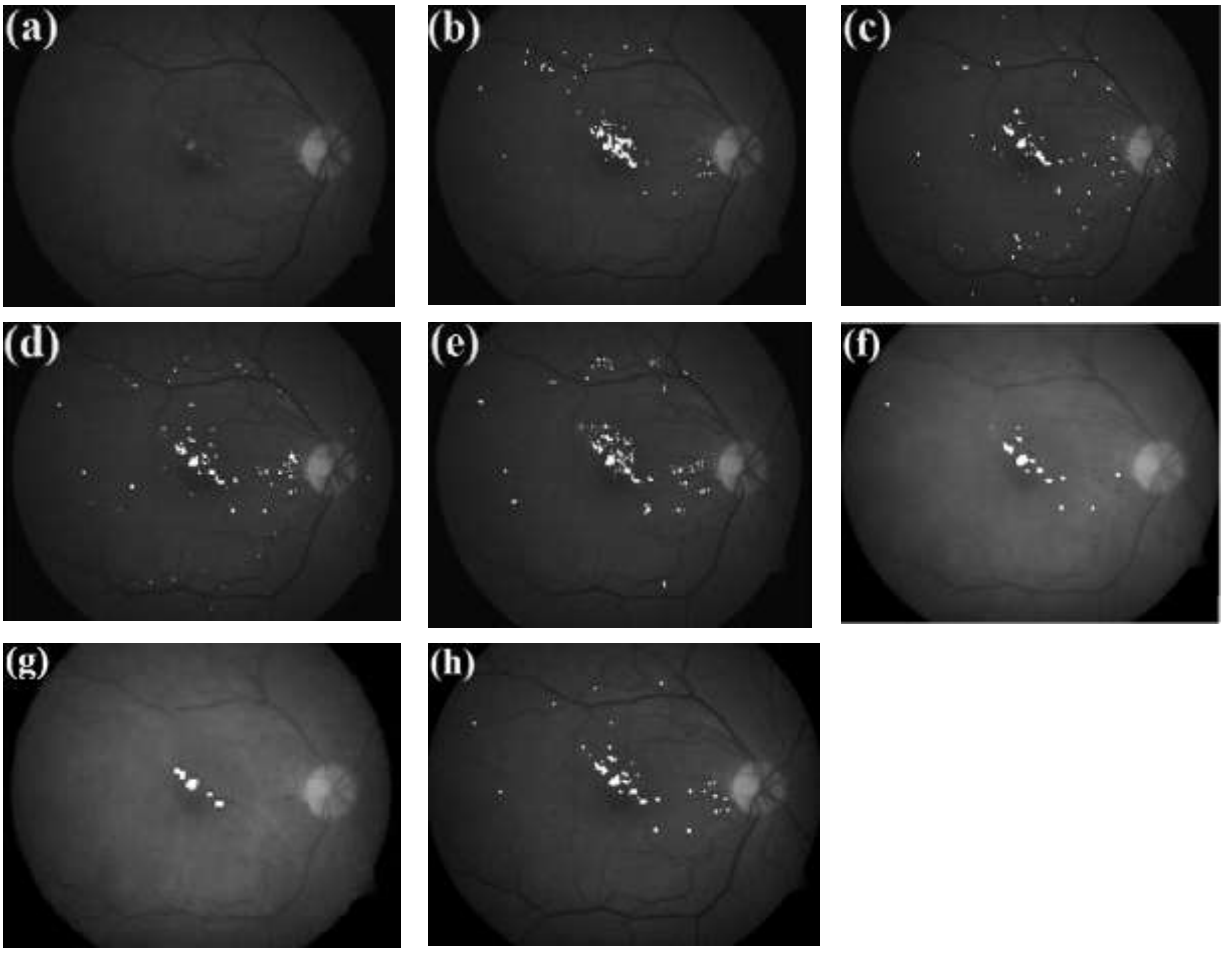

Fig. 13 visual comparison of exudate segmentation methods on first image of DIARETDB1: (a) green plane of the original image that contains exudates; exudate map overlaid on image by (b) manually (ground truth); (c) Sopharak et al.[44]; (d) Walter et al.[51] ; (e) Welfer et al.[52]; (f) Imani et al.[7]; (g) Yang et al.[89] and (h) The proposed BAMCA method

5.4.4 Assessment of separation performance using third party algorithms

Having vessel and exudate components of the retinal images separated, one may decide to use each component for further processing. Hence, in order to evaluate the quality of separated components of the retinal images, in this section we apply third party state-of-the-art segmentation methods to see if excluding non-relevant components from the method can improve it or not, and to what extents. Therefore, two recent successful methods [27], [31] with publicly available implementations[1] are selected along with our previous work [6] on vessel segmentation. Each of these three vessel segmentation methods are studied in two different cases and the results are compared in Table 4: when the original image green plane is input to the method versus the case that only the vessel component of green plane is used as its input. The results indicate that noticeable improvement is achieved when the vessel component is used as input of the segmentation algorithms and the higher accuracy value is reported in this case.

[1] Nguyen method: http://people.eng.unimelb.edu.au/thivun/projects/retinal_segmentation and B-COSFIRE method: https://gitlab.com/nicstrisc/B-COSFIRE-MATLAB

Table 4 Effect of exudate lesion separation on vessel segmentation results

Method		DRIVE			STARE		
		Sen	Spec	Acc	Sen	Spec	Acc
Nguyen et al. [31]	Without separation	-	-	94.07	-	-	93.24
	With separation	76.63	96.98	94.94	80.03	95.40	94.02
B-COSFIRE method [27]	Without separation	76.55	97.64	94.42	77.16	97.01	94.97
	With separation	77.09	97.32	95.28	75.30	97.10	95.14
Imani et al. [6]	Without separation	68.88	98.00	95.01	73.21	97.23	94.95
	With separation	77.59	97.28	95.28	78.62	96.05	95.01

6 Discussion

As described, the proposed BAMCA method simultaneously separates vessel and exudate lesion components from the input retinal image in an iterative procedure. The suggested two-level process of the algorithm lets us properly join the iterative decomposition scheme of MCA, with the adaptive sparse patch-based representation obtained via dictionary learning. Although recently automatic DR grading has seen a noticeable progress with the introduction of deep leaning methods in the field, still there are lots of unsolved challenges in automatic and computerized analysis of retinal images as sources of valuable medical information about the patients. Detecting lesions accurately enough and locating pathological regions at pixel level is yet to be done.

In our research, we focus on decomposition of retinal images into clinically useful components such as vessels and different lesion types; as it can be a prerequisite for providing useful information for the ophthalmologists in performing many medical procedures including diagnosis, treatment selection and other clinical decision making. Hence in this paper, separation of vessels and exudate lesions is studied which our collaborator physicians most needed in their daily jobs in choosing among different treatment methods and convalescent care.

In general, the comparison between different image separation algorithms is done with respect to their application [77]. In our application, two different scenarios may be considered: when the obtained components are supposed to be visually assessed by a specialist physician or when they have to be input to the other automatic processing stages such as segmentation. Both such scenarios are considered in this paper and the obtained results are promising, though still much more efforts are needed in integrating such automations in the clinical procedures.

The reported results of separating vessel and exudate components using BAMCA in Fig. 3 show an important advantage of the proposed approach: the pathological conditions do not have significant effect on the vessel segmentation. Therefore, even thin vessels around the lesions can still be extracted accurately enough which is of great value since such vessels are the first to demonstrate signs of next stages of diabetes. Moreover, the vessels near the optic disk are retrieved well enough, where many traditional vessel segmentation methods produce false results. On the other hand, the reported exudate detection outcome is not sensitive to the size of pathological lesions and hence, as shown in Fig. 3 (e), both small and large exudates are well extracted.

Qualitative visual inspection of the obtained components confirm the effectiveness of the proposed algorithm in separation of vessel and exudate parts even when the retinal image is severely changed from its normal state and get affected by the progress of DR. Since the proposed method is a generative approach which delivers meaningful separated parts of the retinal image, our main achievement is not necessarily surpassing the results of methods originally designed for vessel segmentation or exudate

detection. Nevertheless, we achieved comparable accuracy with state-of-the-art in both tasks and using different datasets.

A strong point of the proposed two-level MCA is setting up an iterative competition between different dictionaries in order to separate existing components of the retinal image. This feature lets the algorithm change its opinion as the separation process progresses. In addition, the flexibility obtained from learning the proper dictionaries greatly help to adapt to very complex target structures which are clinically important. On the other hand, the computation cost and limited number of available training samples severely restricts size and quality of the learned dictionaries. In fact, to capture more complex structures, one needs larger patch sizes and larger number of atoms to obtain proper representation; both of which intensely increase computation costs. Using multiresolution techniques may help but dictionary learning scenarios should also be improved. Another downside of the presented approach is lots of parameters which should be adjusted a priori. What we presented here was a proof of concept, and we do not claim that our parameter settings were optimal. Careful validations are necessary to optimize value of each parameter through experiments and according to well justified approaches in machine learning.

7 Conclusion and future work

In this paper, we proposed a novel framework, called BAMCA, based on extension of MCA algorithm in order to adopt the adaptive representation obtained via dictionary learning. The vessels and exudate lesions were extracted as diagnostically helpful morphological components of the retinal images. An iterative bi-level strategy was presented: each patch is sparsely represented using the offline pre-learnt dictionaries; while image components are gradually taken out in an iterative global competition at image level. As images of single component are not available, the dictionary learning phase was properly customized to use pairs of retinal images and their vessel and lesion maps. Reported results confirmed the effectiveness of the proposed method in the separation of vessel and exudate components even when the retinal image was severely deviated from its normal healthy state and got affected by the progress of DR.

Using the separated vessel component, we could achieve above 95% accuracy in vessel segmentation and also improve third party algorithms by a few percent in accuracy. The resulted exudate component was also successfully used in detection of various size exudates with satisfactory outcome comparable with state-of-the-art.

Extending our method by properly training other lesion-specific dictionaries is our next step. In our future research, we plan to use the proposed approach in developing an automatic screening system which would support the ophthalmologists not only in grading the diabetic retinopathy, but also in deciding about the type and duration of treatment, scheduling patients' arrival to the clinic and other necessary status checks or lab visits. Such system can also be used in training of fresh ophthalmologists and education of residents.

References

[1] W. Soliman, P. Hasler, B. Sander, and M. Larsen, "Local retinal sensitivity in relation to specific retinopathy lesions in diabetic macular oedema," *Acta Ophthalmol. (Copenh.)*, vol. 90, no. 3, pp. 248–253, 2012.

[2] M. Sasaki, R. Kawasaki, J. E. Noonan, T. Y. Wong, E. Lamoureux, and J. J. Wang, "Quantitative Measurement of Hard Exudates in Patients With Diabetes and Their Associations With Serum Lipid Levels," *Investig. Opthalmology Vis. Sci.*, vol. 54, no. 8, p. 5544, Aug. 2013.

[3] S. Chang, L. Vaccarella, S. Olatunji, C. Cebulla, and J. Christoforidis, "Diagnostic Challenges in Retinitis Pigmentosa: Genotypic Multiplicity and Phenotypic Variability," *Curr. Genomics*, vol. 12, no. 4, pp. 267–275, Jun. 2011.
[4] B. Zhang, F. Karray, Q. Li, and L. Zhang, "Sparse representation classifier for microaneurysm detection and retinal blood vessel extraction," *Inf. Sci.*, vol. 200, pp. 78–90, 2012.
[5] M. Javidi, H.-R. Pourreza, and A. Harati, "Vessel segmentation and microaneurysm detection using discriminative dictionary learning and sparse representation," *Comput. Methods Programs Biomed.*, vol. 139, pp. 93–108, 2017.
[6] E. Imani, M. Javidi, and H.-R. Pourreza, "Improvement of retinal blood vessel detection using morphological component analysis," *Comput. Methods Programs Biomed.*, vol. 118, no. 3, pp. 263–279, 2015.
[7] E. Imani and H.-R. Pourreza, "A novel method for retinal exudate segmentation using signal separation algorithm," *Comput. Methods Programs Biomed.*, vol. 133, pp. 195–205, 2016.
[8] G. Peyré, J. Fadili, and J.-L. Starck, "Learning the morphological diversity," *SIAM J. Imaging Sci.*, vol. 3, no. 3, pp. 646–669, 2010.
[9] J. S. Turek, J. Sulam, M. Elad, and I. Yavneh, "Fusion of ultrasound harmonic imaging with clutter removal using sparse signal separation," in *Acoustics, Speech and Signal Processing (ICASSP), 2015 IEEE International Conference on*, 2015, pp. 793–797.
[10] J. S. Turek, M. Elad, and I. Yavneh, "Clutter mitigation in echocardiography using sparse signal separation," *J. Biomed. Imaging*, vol. 2015, p. 9, 2015.
[11] Y. Chen *et al.*, "Artifact suppressed dictionary learning for low-dose CT image processing," *IEEE Trans. Med. Imaging*, vol. 33, no. 12, pp. 2271–2292, 2014.
[12] S. Liu, Y. Xian, H. Li, and Z. Yu, "Text detection in natural scene images using morphological component analysis and Laplacian dictionary," *IEEECAA J. Autom. Sin.*, 2017.
[13] J. Wen, J. Zhao, and C. Wang, "Improved morphological component analysis for interference hyperspectral image decomposition," *Comput. Electr. Eng.*, vol. 46, pp. 394–402, 2015.
[14] N. Deligiannis, J. F. Mota, B. Cornelis, M. R. Rodrigues, and I. Daubechies, "X-ray image separation via coupled dictionary learning," in *Image Processing (ICIP), 2016 IEEE International Conference on*, 2016, pp. 3533–3537.
[15] M. Aharon, M. Elad, and A. Bruckstein, "K-SVD: An algorithm for designing overcomplete dictionaries for sparse representation," *IEEE Trans. Signal Process.*, vol. 54, no. 11, pp. 4311–4322, 2006.
[16] M. M. Fraz *et al.*, "Blood vessel segmentation methodologies in retinal images–a survey," *Comput. Methods Programs Biomed.*, vol. 108, no. 1, pp. 407–433, 2012.
[17] M. R. K. Mookiah, U. R. Acharya, C. K. Chua, C. M. Lim, E. Y. K. Ng, and A. Laude, "Computer-aided diagnosis of diabetic retinopathy: A review," *Comput. Biol. Med.*, vol. 43, no. 12, pp. 2136–2155, 2013.
[18] K. K. Delibasis, A. I. Kechriniotis, C. Tsonos, and N. Assimakis, "Automatic model-based tracing algorithm for vessel segmentation and diameter estimation," *Comput. Methods Programs Biomed.*, vol. 100, no. 2, pp. 108–122, 2010.
[19] E. Grisan, A. Pesce, A. Giani, M. Foracchia, and A. Ruggeri, "A new tracking system for the robust extraction of retinal vessel structure," in *Engineering in Medicine and Biology Society, 2004. IEMBS'04. 26th Annual International Conference of the IEEE*, 2004, vol. 1, pp. 1620–1623.
[20] S. Chaudhuri, S. Chatterjee, N. Katz, M. Nelson, and M. Goldbaum, "Detection of blood vessels in retinal images using two-dimensional matched filters," *IEEE Trans. Med. Imaging*, vol. 8, no. 3, pp. 263–269, 1989.
[21] C. Yao and H. Chen, "Automated retinal blood vessels segmentation based on simplified PCNN and fast 2D-Otsu algorithm," *J. Cent. South Univ. Technol.*, vol. 16, no. 4, pp. 640–646, 2009.
[22] B. Zhang, L. Zhang, L. Zhang, and F. Karray, "Retinal vessel extraction by matched filter with first-order derivative of Gaussian," *Comput. Biol. Med.*, vol. 40, no. 4, pp. 438–445, 2010.

[23] A. D. Hoover, V. Kouznetsova, and M. Goldbaum, "Locating blood vessels in retinal images by piecewise threshold probing of a matched filter response," *IEEE Trans. Med. Imaging*, vol. 19, no. 3, pp. 203–210, 2000.
[24] P. Bankhead, C. N. Scholfield, J. G. McGeown, and T. M. Curtis, "Fast retinal vessel detection and measurement using wavelets and edge location refinement," *PloS One*, vol. 7, no. 3, p. e32435, 2012.
[25] Y. Wang, G. Ji, P. Lin, and E. Trucco, "Retinal vessel segmentation using multiwavelet kernels and multiscale hierarchical decomposition," *Pattern Recognit.*, vol. 46, no. 8, pp. 2117–2133, 2013.
[26] M. U. Akram and S. A. Khan, "Multilayered thresholding-based blood vessel segmentation for screening of diabetic retinopathy," *Eng. Comput.*, vol. 29, no. 2, pp. 165–173, 2013.
[27] G. Azzopardi, N. Strisciuglio, M. Vento, and N. Petkov, "Trainable COSFIRE filters for vessel delineation with application to retinal images," *Med. Image Anal.*, vol. 19, no. 1, pp. 46–57, 2015.
[28] M. E. Martinez-Perez, A. D. Hughes, S. A. Thom, A. A. Bharath, and K. H. Parker, "Segmentation of blood vessels from red-free and fluorescein retinal images," *Med. Image Anal.*, vol. 11, no. 1, pp. 47–61, 2007.
[29] M. Vlachos and E. Dermatas, "Multi-scale retinal vessel segmentation using line tracking," *Comput. Med. Imaging Graph.*, vol. 34, no. 3, pp. 213–227, 2010.
[30] A. Fathi and A. R. Naghsh-Nilchi, "Automatic wavelet-based retinal blood vessels segmentation and vessel diameter estimation," *Biomed. Signal Process. Control*, vol. 8, no. 1, pp. 71–80, 2013.
[31] U. T. Nguyen, A. Bhuiyan, L. A. Park, and K. Ramamohanarao, "An effective retinal blood vessel segmentation method using multi-scale line detection," *Pattern Recognit.*, vol. 46, no. 3, pp. 703–715, 2013.
[32] A. Elbalaoui, M. Fakir, K. Taifi, and A. Merbouha, "Automatic detection of blood vessel in retinal images," in *Computer Graphics, Imaging and Visualization (CGiV), 2016 13th International Conference on*, 2016, pp. 324–332.
[33] G. B. Kande, P. V. Subbaiah, and T. S. Savithri, "Unsupervised fuzzy based vessel segmentation in pathological digital fundus images," *J. Med. Syst.*, vol. 34, no. 5, pp. 849–858, 2010.
[34] S. A. Salem, N. M. Salem, and A. K. Nandi, "Segmentation of retinal blood vessels using a novel clustering algorithm (RACAL) with a partial supervision strategy," *Med. Biol. Eng. Comput.*, vol. 45, no. 3, pp. 261–273, 2007.
[35] M. Niemeijer, J. Staal, B. van Ginneken, M. Loog, M. D. Abramoff, and others, "Comparative study of retinal vessel segmentation methods on a new publicly available database," in *SPIE medical imaging*, 2004, vol. 5370, pp. 648–656.
[36] J. Staal, M. D. Abràmoff, M. Niemeijer, M. A. Viergever, and B. Van Ginneken, "Ridge-based vessel segmentation in color images of the retina," *IEEE Trans. Med. Imaging*, vol. 23, no. 4, pp. 501–509, 2004.
[37] X. You, Q. Peng, Y. Yuan, Y. Cheung, and J. Lei, "Segmentation of retinal blood vessels using the radial projection and semi-supervised approach," *Pattern Recognit.*, vol. 44, no. 10, pp. 2314–2324, 2011.
[38] J. V. Soares, J. J. Leandro, R. M. Cesar, H. F. Jelinek, and M. J. Cree, "Retinal vessel segmentation using the 2-D Gabor wavelet and supervised classification," *IEEE Trans. Med. Imaging*, vol. 25, no. 9, pp. 1214–1222, 2006.
[39] M. S. Miri and A. Mahloojifar, "Retinal image analysis using curvelet transform and multistructure elements morphology by reconstruction," *IEEE Trans. Biomed. Eng.*, vol. 58, no. 5, pp. 1183–1192, 2011.
[40] M. M. Fraz *et al.*, "An approach to localize the retinal blood vessels using bit planes and centerline detection," *Comput. Methods Programs Biomed.*, vol. 108, no. 2, pp. 600–616, 2012.
[41] B. Al-Diri, A. Hunter, and D. Steel, "An active contour model for segmenting and measuring retinal vessels," *IEEE Trans. Med. Imaging*, vol. 28, no. 9, pp. 1488–1497, 2009.
[42] B. S. Lam, Y. Gao, and A. W.-C. Liew, "General retinal vessel segmentation using regularization-based multiconcavity modeling," *IEEE Trans. Med. Imaging*, vol. 29, no. 7, pp. 1369–1381, 2010.

[43] D. Siva Sundhara Raja and S. Vasuki, "Automatic detection of blood vessels in retinal images for diabetic retinopathy diagnosis," *Comput. Math. Methods Med.*, vol. 2015, 2015.
[44] A. Sopharak, B. Uyyanonvara, and S. Barman, "Automatic exudate detection from non-dilated diabetic retinopathy retinal images using fuzzy c-means clustering," *sensors*, vol. 9, no. 3, pp. 2148–2161, 2009.
[45] A. Osareh, B. Shadgar, and R. Markham, "A computational-intelligence-based approach for detection of exudates in diabetic retinopathy images," *IEEE Trans. Inf. Technol. Biomed.*, vol. 13, no. 4, pp. 535–545, 2009.
[46] I. N. Figueiredo, S. Kumar, C. M. Oliveira, J. D. Ramos, and B. Engquist, "Automated lesion detectors in retinal fundus images," *Comput. Biol. Med.*, vol. 66, pp. 47–65, 2015.
[47] A. Rocha, T. Carvalho, H. F. Jelinek, S. Goldenstein, and J. Wainer, "Points of interest and visual dictionaries for automatic retinal lesion detection," *IEEE Trans. Biomed. Eng.*, vol. 59, no. 8, pp. 2244–2253, 2012.
[48] M. U. Akram, A. Tariq, M. A. Anjum, and M. Y. Javed, "Automated detection of exudates in colored retinal images for diagnosis of diabetic retinopathy," *Appl. Opt.*, vol. 51, no. 20, pp. 4858–4866, 2012.
[49] M. U. Akram, S. Khalid, A. Tariq, S. A. Khan, and F. Azam, "Detection and classification of retinal lesions for grading of diabetic retinopathy," *Comput. Biol. Med.*, vol. 45, pp. 161–171, 2014.
[50] Q. Liu *et al.*, "A location-to-segmentation strategy for automatic exudate segmentation in colour retinal fundus images," *Comput. Med. Imaging Graph.*, vol. 55, pp. 78–86, 2017.
[51] T. Walter, J.-C. Klein, P. Massin, and A. Erginay, "A contribution of image processing to the diagnosis of diabetic retinopathy-detection of exudates in color fundus images of the human retina," *IEEE Trans. Med. Imaging*, vol. 21, no. 10, pp. 1236–1243, 2002.
[52] D. Welfer, J. Scharcanski, and D. R. Marinho, "A coarse-to-fine strategy for automatically detecting exudates in color eye fundus images," *Comput. Med. Imaging Graph.*, vol. 34, no. 3, pp. 228–235, 2010.
[53] B. Harangi and A. Hajdu, "Automatic exudate detection by fusing multiple active contours and regionwise classification," *Comput. Biol. Med.*, vol. 54, pp. 156–171, 2014.
[54] X. Zhang *et al.*, "Exudate detection in color retinal images for mass screening of diabetic retinopathy," *Med. Image Anal.*, vol. 18, no. 7, pp. 1026–1043, 2014.
[55] C. Sinthanayothin *et al.*, "Automated detection of diabetic retinopathy on digital fundus images," *Diabet. Med.*, vol. 19, no. 2, pp. 105–112, 2002.
[56] H. Li and O. Chutatape, "Automated feature extraction in color retinal images by a model based approach," *IEEE Trans. Biomed. Eng.*, vol. 51, no. 2, pp. 246–254, 2004.
[57] C. I. Sánchez, M. García, A. Mayo, M. I. López, and R. Hornero, "Retinal image analysis based on mixture models to detect hard exudates," *Med. Image Anal.*, vol. 13, no. 4, pp. 650–658, 2009.
[58] S. Ali *et al.*, "Statistical atlas based exudate segmentation," *Comput. Med. Imaging Graph.*, vol. 37, no. 5, pp. 358–368, 2013.
[59] C. Pereira, L. Gonçalves, and M. Ferreira, "Exudate segmentation in fundus images using an ant colony optimization approach," *Inf. Sci.*, vol. 296, pp. 14–24, 2015.
[60] M. García, C. I. Sánchez, J. Poza, M. I. López, and R. Hornero, "Detection of hard exudates in retinal images using a radial basis function classifier," *Ann. Biomed. Eng.*, vol. 37, no. 7, pp. 1448–1463, 2009.
[61] B. Graham, "Kaggle diabetic retinopathy detection competition report," *Univ. Warwick*, 2015.
[62] G. Quellec, K. Charrière, Y. Boudi, B. Cochener, and M. Lamard, "Deep image mining for diabetic retinopathy screening," *Med. Image Anal.*, vol. 39, pp. 178–193, 2017.
[63] V. Gulshan *et al.*, "Development and validation of a deep learning algorithm for detection of diabetic retinopathy in retinal fundus photographs," *Jama*, vol. 316, no. 22, pp. 2402–2410, 2016.
[64] N. Lunscher, M. L. Chen, N. Jiang, and J. Zelek, "Automated Screening for Diabetic Retinopathy Using Compact Deep Networks," *J. Comput. Vis. Imaging Syst.*, vol. 3, no. 1, 2017.

[65] S. Wan, Y. Liang, and Y. Zhang, "Deep convolutional neural networks for diabetic retinopathy detection by image classification," *Comput. Electr. Eng.*, vol. 72, pp. 274–282, 2018.
[66] "Kaggle Diabetic Retinopathy Detection Competition." [Online]. Available: https://www.kaggle.com/c/diabetic-retinopathy-detection. [Accessed: 09-Feb-2018].
[67] J. Cohen, "Weighted kappa: Nominal scale agreement provision for scaled disagreement or partial credit.," *Psychol. Bull.*, vol. 70, no. 4, p. 213, 1968.
[68] M. E. Gegundez-Arias *et al.*, "A tool for automated diabetic retinopathy pre-screening based on retinal image computer analysis," *Comput. Biol. Med.*, vol. 88, pp. 100–109, 2017.
[69] M. Melinščak, P. Prentašić, and S. Lončarić, "Retinal vessel segmentation using deep neural networks," in *VISAPP 2015 (10th International Conference on Computer Vision Theory and Applications)*, 2015.
[70] D. Maji, A. Santara, P. Mitra, and D. Sheet, "Ensemble of Deep Convolutional Neural Networks for Learning to Detect Retinal Vessels in Fundus Images.," *CoRR*, vol. abs/1603.04833, 2016.
[71] Q. Li, B. Feng, L. Xie, P. Liang, H. Zhang, and T. Wang, "A Cross-Modality Learning Approach for Vessel Segmentation in Retinal Images.," *IEEE Trans Med Imaging*, vol. 35, no. 1, pp. 109–118, 2016.
[72] L. Dai *et al.*, "Clinical Report Guided Retinal Microaneurysm Detection With Multi-Sieving Deep Learning," *IEEE Trans. Med. Imaging*, vol. 37, no. 5, pp. 1149–1161, 2018.
[73] J. Masci, A. Giusti, D. Ciresan, G. Fricout, and J. Schmidhuber, "A fast learning algorithm for image segmentation with max-pooling convolutional networks," in *2013 IEEE International Conference on Image Processing*, 2013, pp. 2713–2717.
[74] Y. Yang, T. Li, W. Li, H. Wu, W. Fan, and W. Zhang, "Lesion detection and grading of diabetic retinopathy via two-stages deep convolutional neural networks," in *International Conference on Medical Image Computing and Computer-Assisted Intervention*, 2017, pp. 533–540.
[75] W. M. Gondal, J. M. Köhler, R. Grzeszick, G. A. Fink, and M. Hirsch, "Weakly-supervised localization of diabetic retinopathy lesions in retinal fundus images," in *Image Processing (ICIP), 2017 IEEE International Conference on*, 2017, pp. 2069–2073.
[76] "Diabetic Retinopathy Detection_Team o_O Solution Summary." [Online]. Available: https://kaggle.com/c/diabetic-retinopathy-detection. [Accessed: 26-Jan-2019].
[77] J.-L. Starck, M. Elad, and D. L. Donoho, "Image decomposition via the combination of sparse representations and a variational approach," *IEEE Trans. Image Process.*, vol. 14, no. 10, pp. 1570–1582, 2005.
[78] J.-L. Starck, M. Elad, and D. Donoho, "Redundant multiscale transforms and their application for morphological component separation," *Adv. Imaging Electron Phys.*, vol. 132, pp. 287–348, 2004.
[79] J. M. Fadili and J.-L. Starck, "Sparse representations and Bayesian image inpainting," in *Proceedings of International Conferences SPARS'05*, 2005, pp. 4–pp.
[80] N. Otsu, "A threshold selection method from gray-level histograms," *IEEE Trans. Syst. Man Cybern.*, vol. 9, no. 1, pp. 62–66, 1979.
[81] K. Zuiderveld, "Contrast limited adaptive histogram equalization," in *Graphics gems IV*, 1994, pp. 474–485.
[82] S. Chen, S. A. Billings, and W. Luo, "Orthogonal least squares methods and their application to non-linear system identification," *Int. J. Control*, vol. 50, no. 5, pp. 1873–1896, 1989.
[83] S. S. Chen, D. L. Donoho, and M. A. Saunders, "Atomic decomposition by basis pursuit," *SIAM Rev.*, vol. 43, no. 1, pp. 129–159, 2001.
[84] J. Bobin, J.-L. Starck, J. M. Fadili, Y. Moudden, and D. L. Donoho, "Morphological component analysis: An adaptive thresholding strategy," *IEEE Trans. Image Process.*, vol. 16, no. 11, pp. 2675–2681, 2007.
[85] T. Kauppi *et al.*, "The DIARETDB1 Diabetic Retinopathy Database and Evaluation Protocol.," in *BMVC*, 2007, pp. 1–10.

[86] "International Council of Ophthalmology : Site Search." [Online]. Available: https://www.icoph.org/site_search.html?cx=006932209847762897769%3Afqedgxt8bto&cof=FORID%3A10&ie=UTF-8&q=diabetic+rethinopathy&x=0&y=0. [Accessed: 10-Mar-2018].
[87] "Diabetic Retinopathy Detection_Data Description." [Online]. Available: https://kaggle.com/c/diabetic-retinopathy-detection. [Accessed: 26-Jan-2019].
[88] "IDRiD - Data_Download." [Online]. Available: https://idrid.grand-challenge.org/Data_Download/. [Accessed: 26-Jan-2019].
[89] N. Yang, H.-C. Lu, G.-L. Fang, and G. Yang, "An effective framework for automatic segmentation of hard exudates in fundus images," *J. Circuits Syst. Comput.*, vol. 22, no. 01, p. 1250075, 2013.